A&A 563, A39 (2014)
DOI: 10.1051/0004-6361/201321736

Astronomy & Astrophysics

The cometary H II regions of DR 21: Bow shocks or champagne flows or both?⋆,⋆⋆

K. Immer⋆⋆⋆,[1,2], C. Cyganowski⋆⋆⋆⋆,[2], M. J. Reid[2], and K. M. Menten[1]

[1] Max-Planck-Institut für Radioastronomie, auf dem Hügel 69, 53121 Bonn, Germany
e-mail: kimmer@mpifr-bonn.mpg.de
[2] Harvard-Smithsonian Center for Astrophysics, 60 Garden Street, MA 02140 Cambridge, USA

Received 19 April 2013 / Accepted 4 January 2014

ABSTRACT

We present deep Very Large Array H66α radio recombination line (RRL) observations of the two cometary H II regions in DR 21. With these sensitive data, we test the "hybrid" bow shock/champagne flow model previously proposed for the DR 21 H II regions. The ionized gas down the tail of the southern H II region is redshifted by up to ~30 km s^{-1} with respect to the ambient molecular gas, as expected in the hybrid scenario. The RRL velocity structure, however, reveals the presence of two velocity components in both the northern and southern H II regions. This suggests that the ionized gas is flowing along cone-like shells, swept-up by stellar winds. The observed velocity structure of the well-resolved southern H II region is most consistent with a picture that combines a stellar wind with stellar motion (as in bow shock models) along a density gradient (as in champagne flow models). The direction of the implied density gradient is consistent with that suggested by maps of dust continuum and molecular line emission in the DR 21 region.

Key words. HII regions – stars: formation – ISM: individual objects: DR21 – ISM: kinematics and dynamics – radio lines: ISM

1. Introduction

There are several models that propose how an H II region may develop a cometary shape. In the "blister" or "champagne flow" models (e.g. Israel 1978; Bodenheimer et al. 1979; Yorke et al. 1983), the ionized gas breaks into the diffuse intercloud medium at the edge of a molecular cloud or flows down a density gradient in the birth cloud of the star. In the bow shock model, the newborn star moves supersonically through the surrounding medium (e.g. Reid & Ho 1985; Mac Low et al. 1991; van Buren & Mac Low 1992). In more recent works, the influence of a strong stellar wind is incorporated into the models (e.g. Gaume et al. 1994; Zhu et al. 2005, 2008; Arthur & Hoare 2006). The stellar wind modifies the structure of the H II region by trapping it in a swept-up shell and forcing ionized flows in that shell. These models make different predictions for the velocity structure of the ionized gas (see Appendix A, included as online material), and so may be tested with spatially resolved radio recombination line (RRL) observations of cometary H II regions.

Cyganowski et al. (2003) (hereafter Paper I) observed the two cometary H II regions in the well-studied DR 21 region in NH_3 and the H53α and H66α radio recombination lines with the Very Large Array (VLA) to investigate whether the gas kinematics were consistent with bow shock or champagne flow models. They found supersonic velocity differences in the ionized gas between the two cometary "heads", and between each "head" and the molecular gas, consistent with simple bow shock models. However, indications of increasing ionized gas velocities (relative to systemic) towards the tail of the southern DR 21 H II region led the authors of Paper I to suggest a "hybrid" model, in which the ionized gas kinematics are bow-shock-like in the cometary head, and champagne-flow-like in the cometary tail (their Fig. 4). More sensitive hydrogen recombination line data were, however, required to probe the velocity field of the ionized gas further down the cometary tail and test the hybrid model. In this paper, we present deep H66α observations of the cometary H II regions in DR 21, obtained with the VLA. These new data are ~3 times more sensitive than the observations of Paper I, allowing us to detect emission further down the tail of the southern H II region.

The paper is structured as follows: in Sect. 2, we describe the observations and we present the results in Sect. 3. In Sect. 4, we compare the results with existing models for cometary H II regions. Complementary observations at infrared and submillimeter wavelengths are presented in Sect. 4.2. Section 5 gives a short summary of the paper.

2. Observations

On July 21 2004, DR 21 was observed in the hydrogen recombination line H66α (rest frequency 22364.17 MHz) using the Very Large Array (VLA)[1] in D configuration. At this frequency, the

⋆ The image cubes are only available as a FITS file at the CDS via anonymous ftp to cdsarc.u-strasbg.fr (130.79.128.5) or via http://cdsarc.u-strasbg.fr/viz-bin/qcat?J/A+A/563/A39

⋆⋆ Table 2, Fig. 4, and Appendices A and B are available in electronic form at http://www.aanda.org

⋆⋆⋆ Member of the International Max Planck Research School (IMPRS) for Astronomy and Astrophysics at the Universities of Bonn and Cologne.

⋆⋆⋆⋆ NSF Astronomy and Astrophysics Postdoctoral Fellow.

[1] The National Radio Astronomy Observatory operates the VLA and is a facility of the National Science Foundation operated under agreement by the Associated Universities, Inc.

VLA had a primary beam size of ∼2′. The pointing center of the observations was $\alpha = 20^h39^m02\overset{s}{.}0$ $\delta = +42°19'42.00''$ (J2000). The total observing time was 9 h with an on-source integration time of approximately 6.3 h. The primary flux calibrator was J1331+305; J2015+371 was observed as the phase calibrator and used for bandpass calibration. The derived flux density of J2015+371 was 2.92 Jy. The bandwidth of the observations was 12.5 MHz, divided into 32 channels, resulting in a spectral resolution of 390.625 kHz/channel (5.2 km s^{-1}/channel). The band center was set to an LSR velocity of −2.0 km s^{-1}. The full width at half maximum (FWHM) size of the synthesized beam was 3.4″. Since our observations are only sensitive on angular scales of less than 60″, smoothly distributed emission at scales larger than ∼0.4 pc was resolved out.

The data reduction was conducted with the NRAO Astronomical Image Processing System (AIPS). After calibration and flagging bad data, we inspected the line data set for spectral channels with no or almost no line emission. Since the radio recombination line is very broad, only a small number of line-free channels were available for spectral baseline determination on the low- (five channels) and high-frequency (two channels) ends of the spectrum. The continuum in the line-free channels was fitted with a flat baseline which was then subtracted from the entire spectrum, yielding a continuum-free line database. Beside the continuum-free line database, a line-free continuum database was constructed from the baseline fit.

The continuum data were self-calibrated, and the solutions transferred to the line data. A *uv* taper was applied to baselines longer than 50 kλ to improve the signal-to-noise ratio and the data were weighted with an AIPS "robust" parameter of 0. The rms of the resulting continuum image, away from sources, is 1 mJy beam^{-1}, and of the line image cube 0.7 mJy beam^{-1} per channel. The continuum image does not reach the thermal noise level because of dynamic range limitations and the effects of poorly-represented large scale structure. The continuum peak is 1722 mJy beam^{-1}, corresponding to a dynamic range of >1700 (compared to a peak of 395 mJy beam^{-1} and dynamic range of ∼560 for the H66α line image cube).

3. Results

Our goal was to obtain more sensitive observations than those presented in Paper I, and in particular to probe the velocity structure of the ionized gas further down the cometary tails to distinguish between the different classes of models for cometary H II regions. A comparison of our continuum image (Fig. 1a) with that in Paper I (their Fig. 2) illustrates the increase in sensitivity. We detect continuum emission ∼0.14 pc further down the tail of the southern H II region[2], increasing its observed east-west extent by ∼50%. The observed head-tail (north-south) extent of the northern H II region is also increased, by about 0.04 pc (∼33%). In addition to tracing ionized gas further down the cometary tails, the sensitivity of the new H66α data also allows the ionized gas kinematics to be studied on smaller spatial scales.

3.1. "Long slit" analysis

With our increased sensitivity, we first extend the "long slit"-style analysis of Paper I to positions further down the tails of the

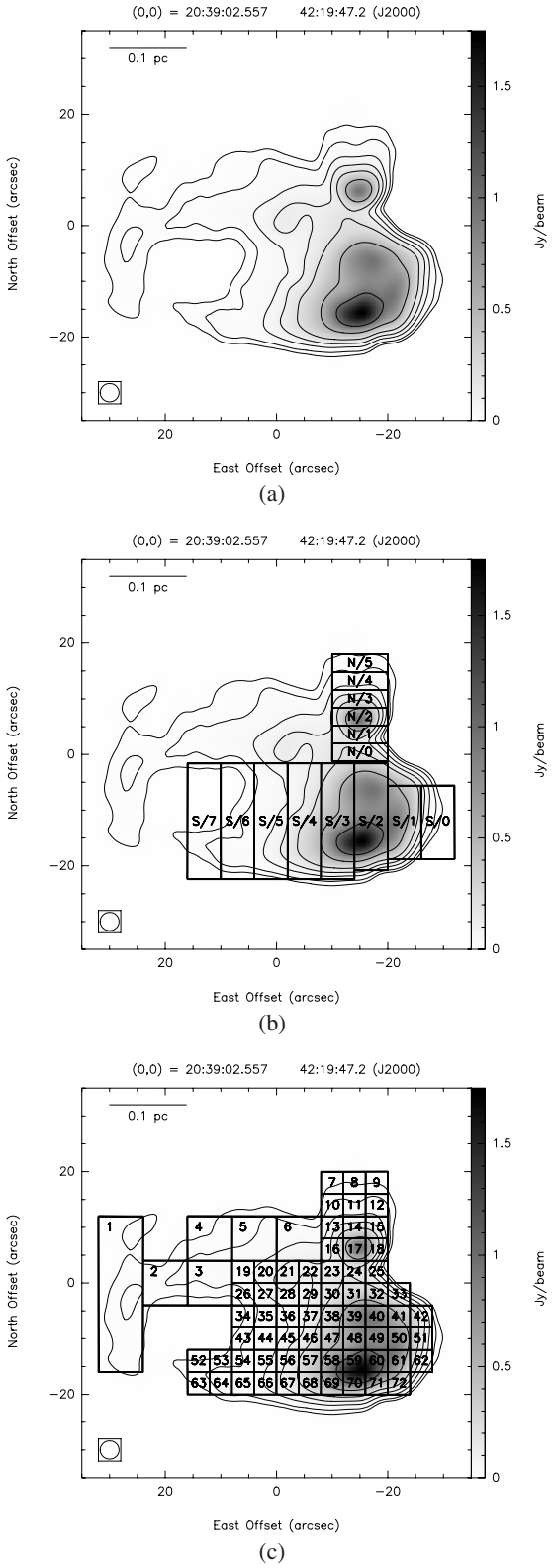

Fig. 1. **a)**: 22 GHz continuum image of the two cometary H II regions in DR 21. The contour levels are 0.01, 0.02, 0.05, 0.1, 0.2, 0.5, and 1 Jy beam^{-1}, chosen to match the contour levels of Fig. 2 in Paper I as closely as possible. (The lowest contour level in Fig. 2 of Paper I is 0.02 Jy beam^{-1}.) **b)** and **c)**: same as **a)**. The boxes show the areas over which the emission was summed to generate the "long slit" **b)** and the "box" **c)** spectra in Figs. 3 and 4. The numbers in the boxes correspond to the position numbers in Tables 1 and 2, respectively. In each panel, the 3.4″ (FWHM) synthesized beam is shown in the lower left corner and a scale bar of 0.1 pc is shown in the upper left corner.

[2] Recent trigonometric parallax observations of 6.7 GHz methanol masers revise the distance to DR21 to 1.5 kpc (Rygl et al. 2012), which we adopt. For a distance of 1.5 kpc, 0.1 pc corresponds to 13.″8.

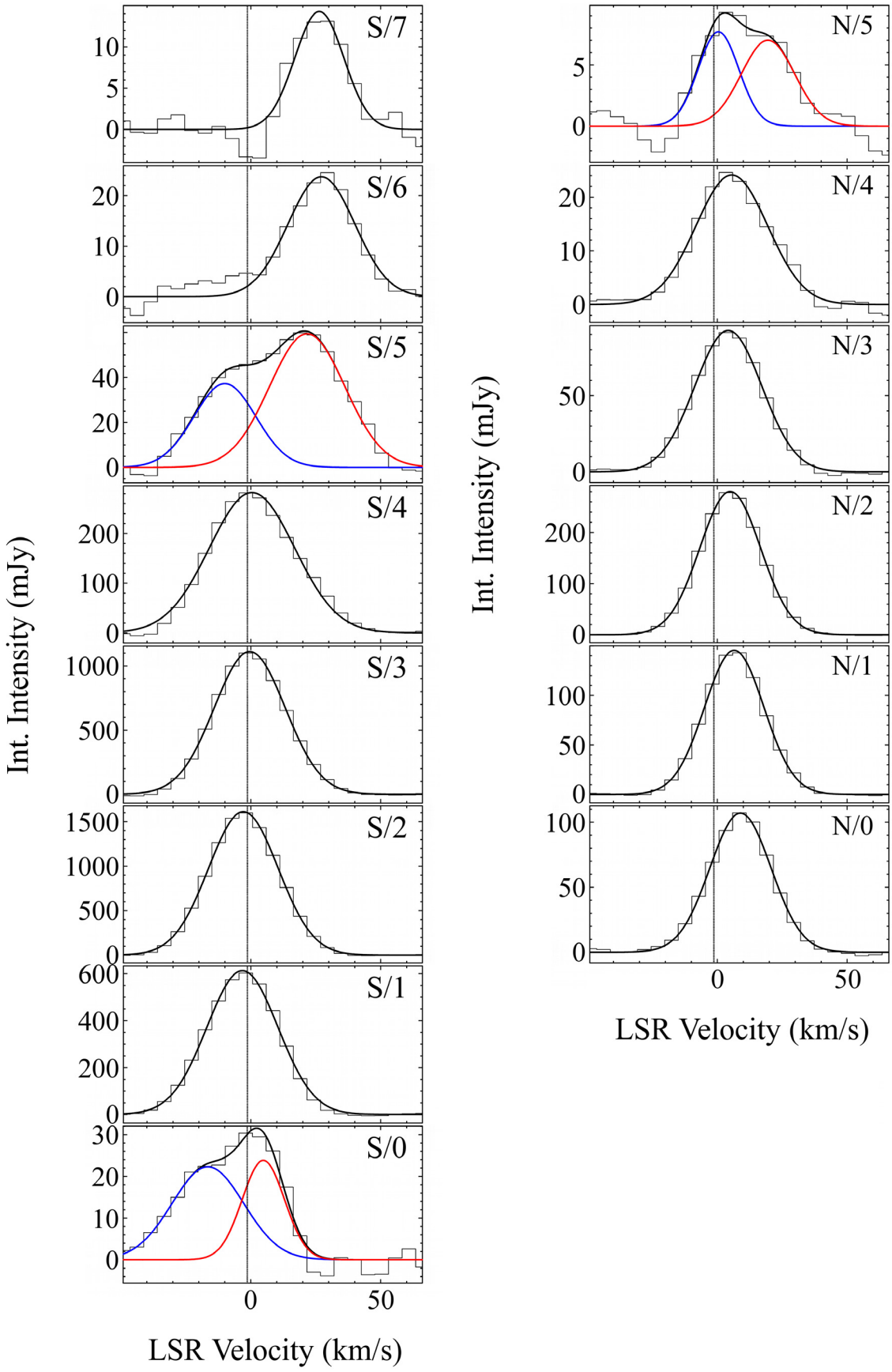

Fig. 2. H66α spectra of the "long slits" (see Fig. 1b). The vertical line marks the systemic velocity of the molecular gas in DR 21, measured from NH_3 (-1.5 km s^{-1}). Positions S/0, S/5, and N/5 clearly show two velocity components, and are fit with two Gaussians. "Gaussian 1", the component with the higher velocity, is shown in red, and "Gaussian 2" in blue (see Table 1). Note that in N/5, both Gaussian 1 and 2 are redshifted with respect to the systemic molecular gas velocity.

Table 1. Fitting results for the "long slit" spectra.

	Gauss 1			Gauss 2			Paper I		
Position	Amplitude (mJy)	Velocity (km s^{-1})	*FWHM* (km s^{-1})	Amplitude (mJy)	Velocity (km s^{-1})	*FWHM* (km s^{-1})	Amplitude (mJy)	Velocity (km s^{-1})	*FWHM* (km s^{-1})
S/0	23.8	4.8	19.2	22.3	−16.5	32.5			
S/1	612.6	−3.3	32.3				398	−2.6	30.9
S/2	1611.1	−2.9	31.6				1132	−2.5	30.9
S/3	1110.9	−0.5	32.2				770	−0.8	31.3
S/4	282.0	0.4	38.7				168	0.2	35.4
S/5	59.3	21.6	34.2	37.2	−10.1	28.2			
S/6	23.7	27.1	30.4						
S/7	14.3	26.3	22.3						
N/0	106.9	8.9	27.8						
N/1	145.4	6.5	26.9				145	5.9	23.9
N/2	280.1	4.9	27.6				186	5.1	26.7
N/3	92.6	4.2	30.4				38	4.1	29.3
N/4	24.1	5.5	32.7				9	−0.5	29.3
N/5	7.0	19.5	24.3	7.7	0.4	18.5			

Notes. The values obtained in Paper I are shown in the last three columns for comparison.

two H II regions. We generated spectra by summing the emission over eight slits in the southern H II region and six slits in the northern H II region (for the positions of the slits, see Fig. 1b). For a better comparison with the results of Paper I, we chose similar sizes and positions for the slits S/1 to S/4 and N/1 to N/4 as in Paper I. Then, we added the slits S/0 (with the same size as S/1, 6″ × 13.2″) at the head of the southern H II region and S/5–S/8 (with the same size as S/4, 6″ × 20.8″) along the tail of the southern H II region. Similarly, we added slits N/0 (with the same size as N/1, 10″ × 3.2″) at the head of the northern H II region, and N/5 (with the same size as N/4, 10″ × 3.2″) at the end of the tail of the northern H II region. Each spectrum was fitted with a Gaussian line profile, yielding the amplitude, the central velocity, and the FWHM of the line. The spectra and the fitting results are shown in Fig. 2 and Table 1, respectively. Our new measurements of the ionized gas velocities are consistent with those of Paper I for seven of the eight common "slits" (S/1–S/4 and N/1–N/3). For slit N/4, we find a central velocity of 5.5 ± 0.4 km s^{-1}, while Paper I reported −0.5 ± 1.6 km s^{-1}. The most likely reason for this discrepancy is the improved sensitivity of the new data. The N/4 H66α detection in Paper I was marginal, with the lowest S/N of the reported fits (Table 1 and compare their Fig. 3 to Fig. 2).

The molecular gas in DR 21 – traced by NH_3 – shows only a small velocity dispersion, with an average systemic velocity of ≈−1.5 km s^{-1} (Paper I). In the northern H II region, the central velocity of the ionized gas at the head is ∼9 km s^{-1} (position N/0). Due to the proximity of the southern H II region, the spectrum at N/0 might be confused by a contribution from the southern H II region. Moving along the tail, the Gaussian shifts blueward until position N/3, then shifts redward at position N/4, where the broader wing at higher positive velocities indicates the presence of a second velocity component. In the spectrum at position N/5, two velocity components can clearly be distinguished. In the southern H II region, the spectrum at the head (S/0) shows two velocity components, one blueshifted at ∼−17 km s^{-1} and one redshifted at ∼5 km s^{-1}. In spectra S/1–S/4, we detect single Gaussians whose central velocities increase (shift redward) along the tail. The spectrum at S/4 shows a broader wing at positive velocities, indicative of a second velocity component; this is supported by the spectrum at S/5, in which the two components can be distinguished. In the spectra at positions S/6 and S/7 we only detect the redshifted velocity component, at large positive velocities (∼27 km s^{-1}).

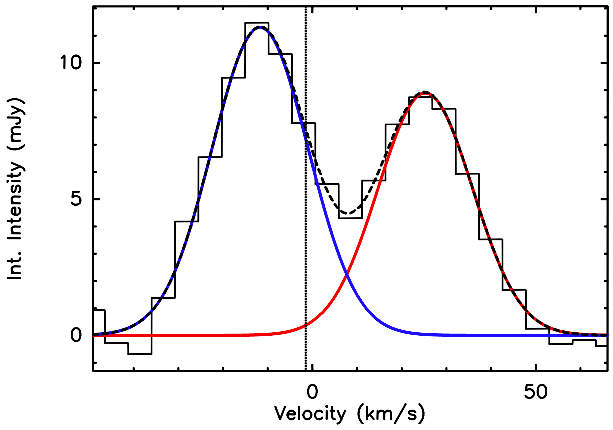

Fig. 3. Example H66α spectrum (position 36). "Gaussian 1", the component with the higher velocity, is shown in red, and "Gaussian 2" in blue (Table 2). The dashed black line presents the sum of the two Gaussian fits. The vertical black line marks the systemic molecular gas velocity of −1.5 km s^{-1}.

3.2. Small-scale kinematics: two velocity components

"Long slit" analysis, such as that employed in Paper I and Sect. 3.1 above, assumes symmetry about the cometary axis. With the higher signal-to-noise ratio of our new data, we can dispense with this assumption and investigate the velocity structure on smaller spatial scales. To do so, we construct a grid of boxes parallel and perpendicular to the major axes of both cometary H II regions. We generated 66 spectra by summing the emission over 4″ × 4″ boxes, chosen to approximately correspond to the area of the synthesized beam. Further along the tail of the southern H II region the emission is weaker; thus, we chose larger boxes (five boxes of 8″ × 8″ and one box of 28″ × 48″) to increase the signal-to-noise ratio. The positions and sizes of the boxes are shown in Fig. 1c. Analyzed on these spatial scales, many of the H66α spectra along the tail of the southern

H II region (positions 3, 4, 5, 19, 20, 27, 28, 35, 36, 44, 45, 55, 63, and 64) clearly show two velocity components. An example (for position 36) is shown in Fig. 3; spectra for all positions are included in Fig. 4.

At the cometary heads, the spectra appear as single Gaussians (Fig. 4); however, a single broad Gaussian can approximate a blend of two narrower Gaussians. The observed linewidths are consistent with two velocity components being present throughout the northern and southern H II regions. Where two clearly separated velocity components are observed, their linewidths are generally close to the thermal linewidth (expected for 8000 K plasma, $FWHM \sim 20$ km s^{-1}). In contrast, where the observed RRL could be interpreted as a single line, the linewidths are broader, consistent with the presence of two, blended velocity components (Fig. 4). We thus fitted all spectra with two Gaussian line profiles to study the distribution of both velocity components over the entire H II regions. However, in ten spectra at the end of the tail of the southern H II region (positions 1, 2, 26, 34, 43, 52, 53, 54, 65, and 67), the second velocity component is too weak to be a 3σ detection. Therefore, we fitted these spectra with only one Gaussian. The fitting results are summarized in Table 2 (available in the electronic edition), and the Gaussian fits are overlaid on the spectra in Figs. 3 and 4.

The central velocities of the two fitted Gaussian components are shown in Fig. 5. Throughout this paper, we refer to the higher-velocity component as "Gaussian 1" (Fig. 5a) and the lower-velocity component as "Gaussian 2" (Fig. 5b)[3]. The positions of the dots in Fig. 5 correspond to the centers of the 72 boxes described above; the dot size scales logarithmically with the amplitude of the Gaussian. The velocity of the ionized material spans a range of ~39 km s^{-1} (−2.4 to 36.6 km s^{-1}) in Gaussian 1 and ~36 km s^{-1} (−28.1 to 7.5 km s^{-1}) in Gaussian 2. Figure 5c plots the velocity difference between the two Gaussian components ($v_{\rm Gauss1} - v_{\rm Gauss2}$), showing that the two velocity components are more separated further down the tails of both H II regions. Figure 5d illustrates asymmetries in the velocity structure: in this panel, the color scale represents $|v_{\rm Gauss1} - v_{\rm sys}| - |v_{\rm Gauss2} - v_{\rm sys}|$ (see also Sect. 4).

In the southern H II region, emission at velocities close to the systemic velocity is detected in the vicinity of the continuum emission peak for Gaussian 1 (Fig. 5a and Table 2, e.g. positions 49, 60, 71). Single-peaked Gaussian line profiles at the head indicate that the velocity difference between the two components is small (see Fig. 4). Down the tail of the southern H II region, the velocity difference increases, with the velocities of Gaussian 1 and 2 reaching +37 km s^{-1} and −28 km s^{-1}, respectively (Fig. 5c). The maximum velocities of the two components near the head are 7 (Pos. 51) and −18 km s^{-1} (Pos. 42) for Gaussian 1 and 2, respectively.

In the northern H II region, velocity components close to the systemic velocity are also detected around the continuum emission peak, near the head of the cometary H II region. Here again, the spectra show single broad Gaussians, approximating a blend of two narrower Gaussians close in velocity. Down the tail, the velocity of Gaussian 1 increases to ~25 km s^{-1} (positions 8 and 11). Notably, our high spatial resolution analysis reveals a velocity gradient of $\gtrsim$8 km s^{-1} *across* the flow, seen in both Gaussian components (e.g. positions 10–12 and 7–9). This velocity gradient is also evident in Fig. 6, which presents the moment 1 map of the northern cometary H II region. Figure 6 shows that the northeastern part of the northern H II region is dominated by emission at large positive velocities, while emission at negative velocities peaks to the northwest.

4. Discussion

4.1. Kinematics of the DR21 cometary H II regions

In our H66α observations, we clearly detect two separate velocity components in the radio recombination line in the tails of the northern and southern DR 21 H II regions (Sect. 3.2). To our knowledge, this is the first time two velocity components have been detected in RRLs over large areas of cometary H II regions. The two velocity components suggest the presence of strong stellar winds, causing the ionized gas to flow along cone-like shells (with the interior of the cone being filled with low-density gas or completely devoid of material; see also Appendix A). Thus, the two velocity components of the radio recombination line are emitted by denser gas at the front and the back of the cone.

Our H66α data provide a direct test of the "hybrid" bow shock/champagne flow model, proposed in Paper I. Long-slit analysis of the well-resolved southern H II region (Sect. 3.1) shows that the velocity of the ionized gas: (i) is blueshifted with respect to the ambient molecular material near the cometary head (S/1); (ii) transitions to being redshifted relative to the ambient molecular gas around positions S/3-S/4; and (iii) is increasingly redshifted relative to the ambient molecular gas further down the cometary tail (S/5-S/7). Our grid-based kinematic analysis (Sect. 3.2) further shows (iv) that the ionized gas at the easternmost extent of the southern H II region's cometary tail is highly redshifted, by ~30 km s^{-1} with respect to the ambient molecular gas. Our data thus confirm that the ionized gas velocity "drifts past" the molecular gas velocity around position S/4 (i and ii, above), as suggested in Paper I. The detection of increasingly redshifted gas further down the tail (iii and iv) – beyond the region studied in Paper I – is strong evidence in support of a hybrid model, which predicts champagne-flow-like kinematics in the cometary tail.

The schematic "hybrid" model proposed in Paper I is consistent with the overall velocity structure of our data, as outlined above. Importantly, however, the hybrid model does not explain the two detected velocity components, since it does not include a confining mechanism such as provided by a stellar wind. In the following, we will assume that the stellar wind scenario is the best explanation for the detected velocity structure in DR 21. The widespread detection of two velocity components in RRLs is an important observational constraint for cometary H II region modeling, as it excludes models that do not incorporate a stellar wind (e.g. the "pure" champagne flow case considered by Arthur & Hoare 2006; Zhu et al. 2008, see also Appendix A). In the southern DR21 H II region, from the continuum emission peak of the ionized gas down to the end of the tail, the absolute velocities of the ionized gas increase. A champagne flow fits best to explain this velocity distribution, with the flow of the ionized gas being accelerated down the density gradient of the surrounding material. Molecular line observations of DR 21 indicate a density gradient in the southern H II region's surrounding environment, as discussed below (Sect. 4.2). Consistent with Paper I, we find lower velocities than the systemic velocity in the head of the H II region, consistent with a bow shock evoked by the movement of the exciting star through dense material. In sum, the velocity structure of the southern H II region is best explained by a champagne flow + stellar wind + bow shock model (such

[3] Note that while Gaussians 1 and 2 are plotted in red and blue, respectively, in Fig. 4, both components may be red- or blue-shifted with respect to the systemic molecular gas velocity: see Figs. 5a,b and Table 2.

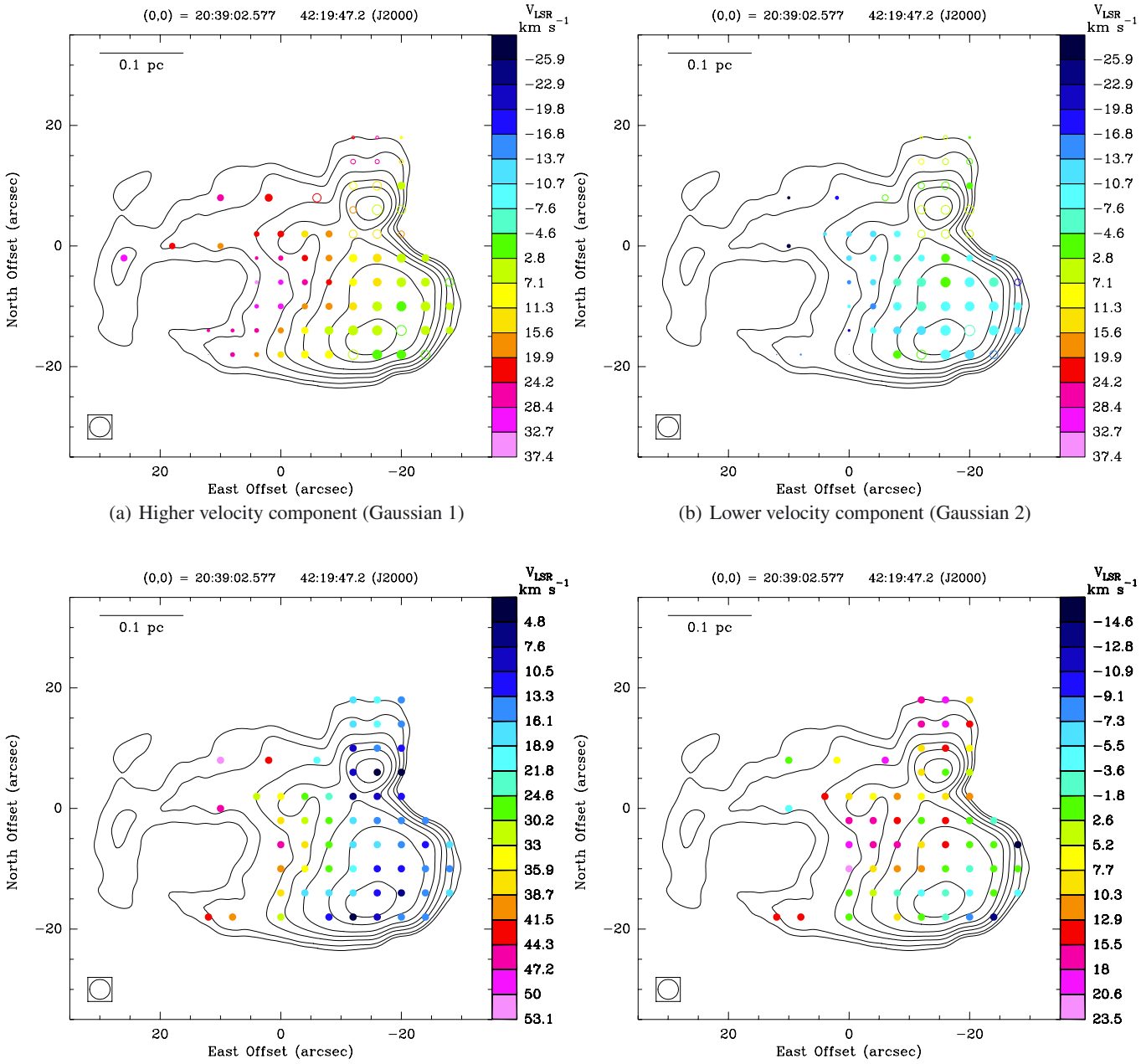

(a) Higher velocity component (Gaussian 1)

(b) Lower velocity component (Gaussian 2)

(c) Velocity difference of the two fitted Gaussians ($v_{Gauss1} - v_{Gauss2}$)

(d) Difference in the offset from the systemic velocity of the two fitted Gaussians ($|v_{Gauss1} - v_{sys}| - |v_{Gauss2} - v_{sys}|$)

Fig. 5. 22 GHz continuum map of DR 21 (contours; same as Fig. 1). The dots represent the Gaussian fitting results; their positions correspond to the centers of the boxes. The systemic velocity of the molecular material is ≈ -1.5 km s^{-1} (green in the *upper panels*). **a)–b)** The dot size scales logarithmically with the amplitude of the Gaussians. **c)** The color of the dots represents the velocity difference between the two Gaussian components. The figure shows that the velocity difference between the two components increases from the head down the tail in both H II regions. **d)** The color of the dots represents $|v_{Gauss1} - v_{sys}| - |v_{Gauss2} - v_{sys}|$, an indication of asymmetry in the velocity structure of the ionized gas (see also Sect. 4). In each panel, the synthesized beam is shown in the lower left corner, and a scale of 0.1 pc is indicated in the upper left corner.

as models G, H, and I of Arthur & Hoare 2006, see Appendix A for more details).

4.1.1. Using kinematics to constrain orientation: southern H II region

Detailed analysis of the two velocity components also allows us to constrain the orientation of the southern H II region. If the southern H II region was seen side-on, i.e. with a cometary axis perpendicular to the line-of-sight, we would expect the velocities of the two Gaussian components to be symmetric with respect to the systemic velocity of −1.5 km s^{-1} (Fig. 46 and 47 of Zhu et al. 2008). This is shown schematically in the left panel of Fig. 7, which presents three lines of sight through a cometary H II region which is shaped by a bow shock, champagne flow, and stellar wind and is viewed side-on. For each line of sight, the expected velocity profile is presented (comprised of a Gaussian component from the front and from the back of the swept-up shell). Since for this inclination the velocities of the

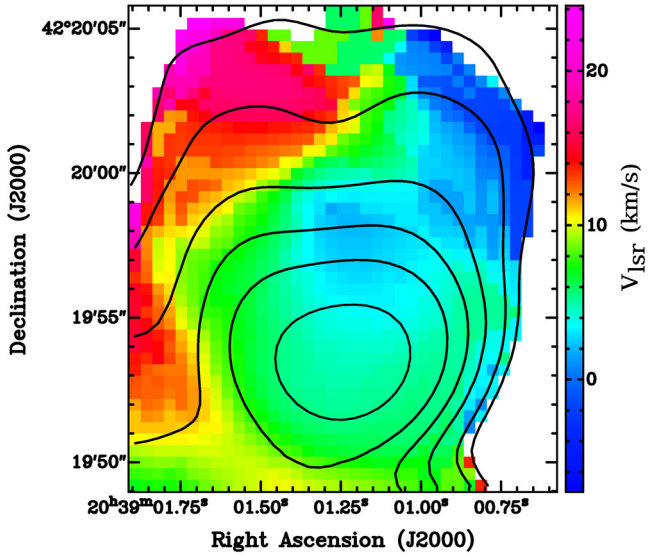

Fig. 6. H66α moment 1 map of the northern H II region in DR 21. A velocity gradient from the eastern to the western side of the cometary H II region is detected.

two components are symmetric relative to the systemic velocity (dashed line), the difference ($|v_{\rm Gauss1} - v_{\rm sys}| - |v_{\rm Gauss2} - v_{\rm sys}|$) would be approximately zero at each position along the H II region. This velocity difference for the two velocity components in the southern H II region is plotted in Fig. 5d. We see that the difference is not close to zero at most positions in the H II region. Close to the continuum emission peak of the ionized gas and in the head of the H II region, the velocity difference is slightly negative, i.e. the velocity difference between Gaussian 2 and the systemic velocity is larger than the difference between Gaussian 1 and the systemic velocity. Down the champagne flow, the velocity difference is positive at most positions, i.e. the velocity offset of Gaussian 1 relative to the systemic velocity is here larger than the velocity offset of Gaussian 2.

Since, at the head, the blueshifted spectral line seems to be emitted closer to the ionization front than the redshifted spectral line and, in the tail, we observe emission further down the flow for the redshifted Gaussian (i.e. at higher velocities) than for the blueshifted Gaussian, we conclude that the cometary axis of the southern H II region has an angle of <90° to the line-of-sight. This is shown schematically in the right panel of Fig. 7 for a cometary H II region whose cometary axis has an angle of 75° to the line-of-sight. Again, the two velocity components from the two sides of the shell are shown for three lines of sight. From the central velocities of the two Gaussian components, we estimate an inclination range of 50°–80° of the cometary axis to the line-of-sight (see Fig. 5a, b, and d). These suggested inclinations for the H II region indicate that the exciting star is moving towards us, consistent with the blueshifted ionized gas velocities near the cometary head.

4.1.2. A rotating ionized flow?: northern H II region kinematics

The absolute velocities of the ionized material in the northern H II region appear to increase down the tail, showing evidence of a champagne flow. The ionized gas velocity at the cometary head is redshifted relative to the systemic velocity of the molecular gas, by up to ~10 km s^{-1} (see also Sect. 3 and Table 2). This is evidence for a bow-shock contribution to the velocity structure near the cometary head (consistent with the results of Paper I). We note, however, that the identification of velocity components at the head of the northern H II region is complicated by the superposition of the velocity components from the two H II regions. At positions 16–18 and 23–25, we attempted to fit the spectra with four Gaussians. The quality of the fits was not encouraging due to the low signal-to-noise ratio; thus, we only show the two Gaussian fits for these positions.

The detection of two velocity components again indicates the presence of a conical ionized shell, confined by a stellar wind, as for the southern H II region. In addition, we detected a velocity gradient *across* the ionized flow, from the eastern to the western side of the northern H II region (Fig. 6). A rotating star with a rotating stellar wind might force the ionized gas in the wind swept-up shell to follow the rotation. This interesting possibility warrants further investigation; however, higher spatial resolution data are required to better constrain the velocity structure.

4.2. Evidence for a density gradient in DR 21

As discussed in Sect. 4, the ionized gas kinematics of the DR 21 H II regions indicate a champagne flow contribution to the cometary tails. Champagne flows require a density gradient in the surrounding medium. Recent large-scale studies of the DR 21 region in (sub)millimeter continuum and molecular line emission provide insight into the interaction of the H II regions with their environment. Davis et al. (2007) mapped the DR 21 region in 870 μm dust continuum emission with the Submillimeter Common User Bolometer Array (SCUBA) on the *James Clerk Maxwell* Telescope (JCMT) (Fig. 8). The half power beam width (HPBW) of the SCUBA observations is 15″. The 870 μm image shows that the head of the southern H II region is embedded in a dust core with a size of ~0.2 × 0.12 pc (27″ × 16″, Davis et al. 2007; Di Francesco et al. 2008). The peak of the submillimeter emission is slightly offset (by ~0.04 pc in the north-west direction) from the peak of the ionized emission.

In Schneider et al. (2010), the emission of several molecular lines (^{12}CO(2–1), ^{13}CO(2–1), HCO$^+$(1–0), H^{13}CO$^+$(1–0), $H_2CO(3_{1,2}–2_{1,1})$, C^{34}S (2–1), and N_2H^+(1–0)) was observed with the IRAM 30 m telescope towards DR 21 with a HPBW between 11″ and 29″. Channel maps of ^{13}CO, H^{13}CO$^+$, and C^{34}S confirm the small velocity dispersion of the molecular gas in DR 21 (their Fig. 7). Velocity-integrated line maps of HCO$^+$ and ^{13}CO show emission of low-density gas from the whole DR 21 region and the associated outflow. In contrast, C^{34}S and N_2H^+ emission, which trace higher density gas, are only observed towards the central part of DR 21, roughly coincident with the SCUBA core. (There is also some weak C^{34}S emission extending to the west.) Neither C^{34}S nor N_2H^+ is detected at the end of the tail of the southern H II region, consistent with a density gradient in the molecular material surrounding the southern H II region with density decreasing from W (cometary head) to E (tail).

5. Conclusion

We have obtained deep H66α radio recombination line observations of the two cometary H II regions in DR 21, with the aim of testing proposed models for cometary H II region kinematics, in particular the "hybrid" bow shock/champagne flow model proposed in Paper I. Our analysis of the velocities of the cometary

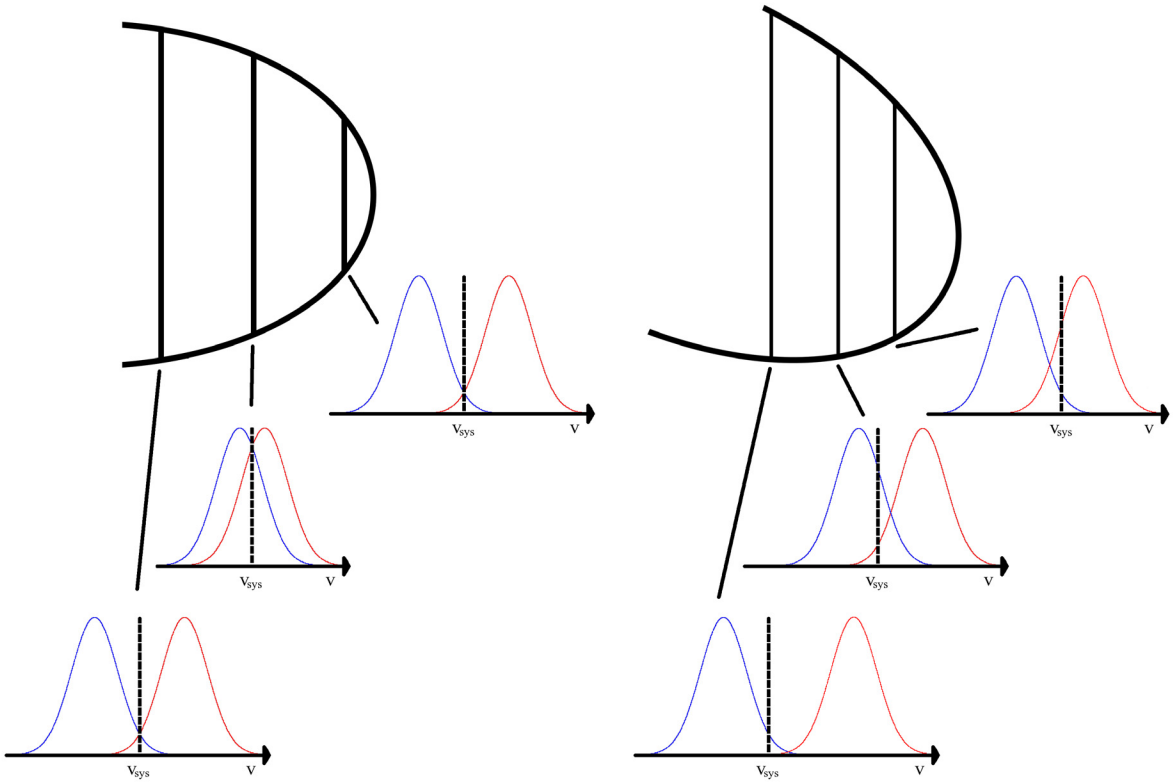

Fig. 7. Schematic diagram showing the effect of orientation on observed ionized gas velocities for a cometary H II region shaped by a bow shock, champagne flow, and strong stellar wind. Due to the stellar wind, the ionized gas is confined to a swept-up shell, which gives rise to two velocity components. The two expected Gaussians components (from the near and far sides of the shell) are sketched for three different lines of sight. In the case of 90° inclination (w.r.t. the line of sight), the two velocity components are emitted at corresponding positions on the sides of the shell, so the velocities are symmetric with respect to the systemic velocity (*left panel*). However, in the case of 75° inclination (w.r.t the line of sight), the two components come from shifted positions along the shell and thus, the offset from the systemic velocity is not the same for the two components (*right panel*). The second case reflects the velocity structure of the southern H II region, suggesting that the exciting star is moving towards us.

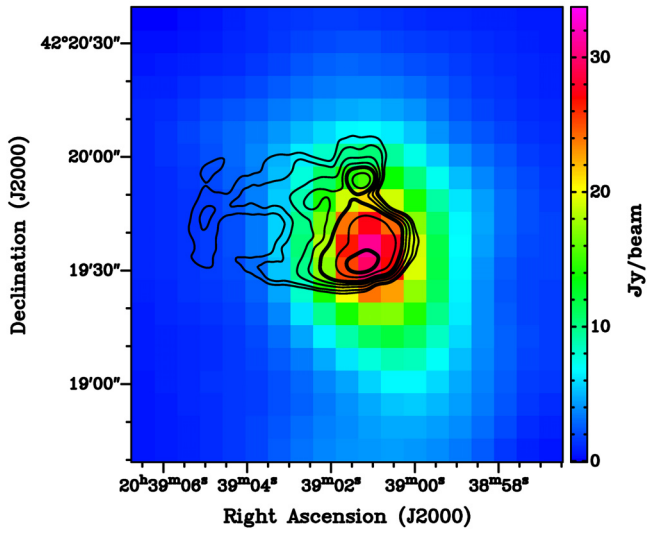

Fig. 8. SCUBA 870 μm image of DR 21 with a HPBW of 15″ (Davis et al. 2007). The contours show the 22 GHz continuum emission with the contour levels corresponding to the contours in Fig. 1. The offset between the submillimeter and radio continuum emission peaks is ~0.04 pc.

heads is consistent with the results of Paper I: we find offsets between the velocities of the ionized gas and the ambient molecular material, indicative of stellar motion as in bow shock models. With the increased sensitivity of the new data, we study the kinematics of the ionized gas along the cometary tails, and find velocities increasing with distance from the cometary heads. In the new data, we detect RRL emission at the extreme eastern end of the tail of the southern H II region, at velocities redshifted by up to ~30 km s^{-1} with respect to the ambient molecular gas. This velocity structure is consistent with a champagne flow contribution in the tail, as in the hybrid scenario.

The sensitivity of the new data allows us to move beyond "long slit" analysis (which assumes symmetry about the cometary axis) and probe the velocity structure on ~4″ scales. A detailed analysis of the ionized gas kinematics clearly shows that two velocity components are widespread in both the northern and southern H II regions. To our knowledge, these are the first observations of cometary H II regions in which two velocity components, belonging to the same region, have been detected in RRLs.

The two velocity components indicate that the ionized gas is likely confined to a thin conical or paraboloidal shell, as predicted by models that include strong stellar winds. Our data suggest that the combined effects of a stellar wind, stellar motion (as in bow shock models) and an ambient density gradient (as in champagne flow models) are necessary to explain the observed ionized gas kinematics. Recent observations of dense gas tracers in the DR 21 region are consistent with the ambient density gradient inferred from the ionized gas kinematics: the cometary head of the southern H II region is embedded in a dense core, while no emission from dense gas tracers is detected towards

the eastern end of the cometary tail. Intriguingly, in the northern H II region we also find tentative evidence for a velocity gradient *across* the flow of the ionized material, which might indicate a rotation of the flow. Higher spatial resolution data are required to investigate this possibility.

Acknowledgements. K.I. would like to thank M. Hoare for fruitful discussions. This research has made use of NASA's Astrophysics Data System Bibliographic Services. C.J.C. is supported by an NSF Astronomy and Astrophysics Postdoctoral Fellowship under award AST-1003134.

References

Arthur, S. J., & Hoare, M. G. 2006, ApJS, 165, 283
Bodenheimer, P., Tenorio-Tagle, G., & Yorke, H. W. 1979, ApJ, 233, 85
Cyganowski, C. J., Reid, M. J., Fish, V. L., & Ho, P. T. P. 2003, ApJ, 596, 344
Davis, C. J., Kumar, M. S. N., Sandell, G., et al. 2007, MNRAS, 374, 29
Di Francesco, J., Johnstone, D., Kirk, H., MacKenzie, T., & Ledwosinska, E. 2008, ApJS, 175, 277
Gaume, R. A., Fey, A. L., & Claussen, M. J. 1994, ApJ, 432, 648
Israel, F. P. 1978, A&A, 70, 769
Mac Low, M.-M., van Buren, D., Wood, D. O. S., & Churchwell, E. 1991, ApJ, 369, 395
Reid, M. J., & Ho, P. T. P. 1985, ApJ, 288, L17
Rygl, K. L. J., Brunthaler, A., Sanna, A., et al. 2012, A&A, 539, A79
Schneider, N., Csengeri, T., Bontemps, S., et al. 2010, A&A, 520, A49
van Buren, D., & Mac Low, M.-M. 1992, ApJ, 394, 534
Yorke, H. W., Tenorio-Tagle, G., & Bodenheimer, P. 1983, A&A, 127, 313
Zhu, Q.-F., Lacy, J. H., Jaffe, D. T., Richter, M. J., & Greathouse, T. K. 2005, ApJ, 631, 381
Zhu, Q.-F., Lacy, J. H., Jaffe, D. T., Richter, M. J., & Greathouse, T. K. 2008, ApJS, 177, 584

Pages 10 to 22 are available in the electronic edition of the journal at http://www.aanda.org

Table 2. Gaussian fitting results.

	Gauss 1			Gauss 2		
Position	Amplitude (mJy)	Velocity (km s^{-1})	*FWHM* (km s^{-1})	Amplitude (mJy)	Velocity (km s^{-1})	*FWHM* (km s^{-1})
POS 1	16.0	29.0	37.8			
POS 2	10.9	23.4	32.6			
POS 3[a]	10.2	19.3	43.9	4.6	−26.5	9.9
POS 4[a]	15.8	24.7	24.8	3.4	−28.1	24.7
POS 5[a]	32.1	22.3	26.5	4.3	−19.7	22.6
POS 6	41.3	21.6	28.2	9.9	1.8	34.6
POS 7[a]	2.4	24.1	13.1	2.8	7.1	22.4
POS 8[a]	2.4	25.2	14.0	4.3	5.1	19.9
POS 9[b]	2.7	10.1	24.2	2.9	−4.5	12.5
POS 10	4.8	24.3	17.0	7.7	7.4	24.4
POS 11[b]	3.8	25.4	13.7	9.5	5.0	27.5
POS 12	3.4	13.9	32.1	9.7	−1.0	24.0
POS 13	18.7	11.2	28.3	10.9	2.6	25.9
POS 14	53.9	13.6	23.6	27.1	−0.5	26.5
POS 15	32.5	7.0	26.7	16.0	−4.4	25.1
POS 16	13.3	16.3	28.2	40.9	6.1	26.1
POS 17	151.1	5.7	28.5	69.7	3.4	24.4
POS 18	48.2	6.6	29.0	50.2	2.9	24.3
POS 19[a]	7.4	21.1	21.4	4.3	−11.2	40.3
POS 20[a]	12.8	20.1	28.7	8.6	−13.0	33.1
POS 21[b]	17.4	14.1	39.1	13.5	−11.1	25.5
POS 22[b]	17.2	16.4	34.7	15.2	−7.8	26.3
POS 23	26.2	12.1	27.2	21.7	5.2	34.6
POS 24	44.2	13.0	24.0	41.0	3.4	23.3
POS 25	9.7	16.2	20.4	23.6	4.1	24.8
POS 26	3.0	27.2	23.2			
POS 27[a]	6.1	25.5	28.4	8.1	−12.2	26.9
POS 28[a]	11.1	21.6	29.3	16.5	−8.7	26.1
POS 29[b]	14.0	18.3	27.0	23.9	−7.1	23.9
POS 30	49.0	8.0	33.0	16.2	−9.5	22.8
POS 31	57.7	12.4	25.7	62.5	−1.6	29.0
POS 32	90.1	5.7	27.2	16.1	−7.9	33.8
POS 33	31.0	4.5	24.3	7.7	−10.8	32.2
POS 34	3.4	36.4	20.0			
POS 35[a]	6.3	31.0	20.9	4.6	−14.1	20.7
POS 36[a]	8.9	25.2	24.9	11.3	−11.7	25.4
POS 37	9.0	19.9	25.0	37.2	−7.2	26.7
POS 38	33.0	11.2	27.2	90.6	−5.2	26.3
POS 39	58.4	14.2	23.5	203.0	−3.5	27.6
POS 40	134.6	5.4	27.4	153.5	−8.4	27.2
POS 41	66.3	5.5	22.9	104.4	−7.2	29.2
POS 42	37.9	−2.0	26.1	13.6	−18.4	28.1
POS 43	4.4	29.6	22.0			
POS 44[a]	8.6	29.6	26.0	3.8	−9.4	29.3
POS 45[a]	9.8	19.6	37.5	11.1	−14.3	28.4
POS 46	17.4	18.0	31.6	46.7	−9.0	28.7
POS 47	34.8	14.7	28.6	122.3	−6.0	26.8
POS 48	137.4	4.4	28.2	124.3	−8.2	25.4
POS 49	190.9	2.5	26.3	125.1	−8.9	26.0
POS 50	144.7	5.0	24.0	129.0	−9.7	26.6
POS 51	27.4	7.0	22.7	37.5	−8.5	30.6
POS 52	2.9	27.1	22.3			
POS 53	3.4	25.4	21.0			
POS 54	4.8	24.4	30.4			
POS 55[a]	9.6	17.0	41.7	3.0	−20.8	20.2
POS 56	19.6	9.3	40.5	12.7	−9.5	32.3
POS 57	59.6	5.8	36.1	33.7	−11.3	27.6
POS 58	181.4	5.4	29.9	75.5	−12.8	23.0
POS 59	218.5	2.8	28.0	258.5	−9.4	26.4
POS 60	160.8	−2.0	30.5	222.4	−7.0	29.9
POS 61	90.9	6.1	23.0	158.9	−9.0	28.0

Notes. [(a)] Two velocity components visible. [(b)] Asymmetric line profile indicates two velocity components.

Table 2. continued.

	Gauss 1			Gauss 2		
Position	Amplitude (mJy)	Velocity (km s^{-1})	*FWHM* (km s^{-1})	Amplitude (mJy)	Velocity (km s^{-1})	*FWHM* (km s^{-1})
POS 62	22.0	5.5	22.3	21.6	−12.3	27.7
POS 63[a]	1.7	27.6	26.4	2.3	−15.8	15.6
POS 64[a]	5.0	24.7	44.3	2.6	−14.5	11.5
POS 65	5.4	18.6	43.6			
POS 66	12.7	14.8	36.2	2.2	−16.0	17.8
POS 67	31.7	7.5	36.2			
POS 68	43.3	8.1	30.3	46.3	−2.7	27.3
POS 69	121.1	3.0	27.5	80.1	1.0	31.8
POS 70	176.8	2.1	28.1	161.2	−7.7	28.2
POS 71	115.3	1.5	29.6	109.3	−12.6	25.2
POS 72	57.6	−2.2	26.7	33.1	−16.3	22.2

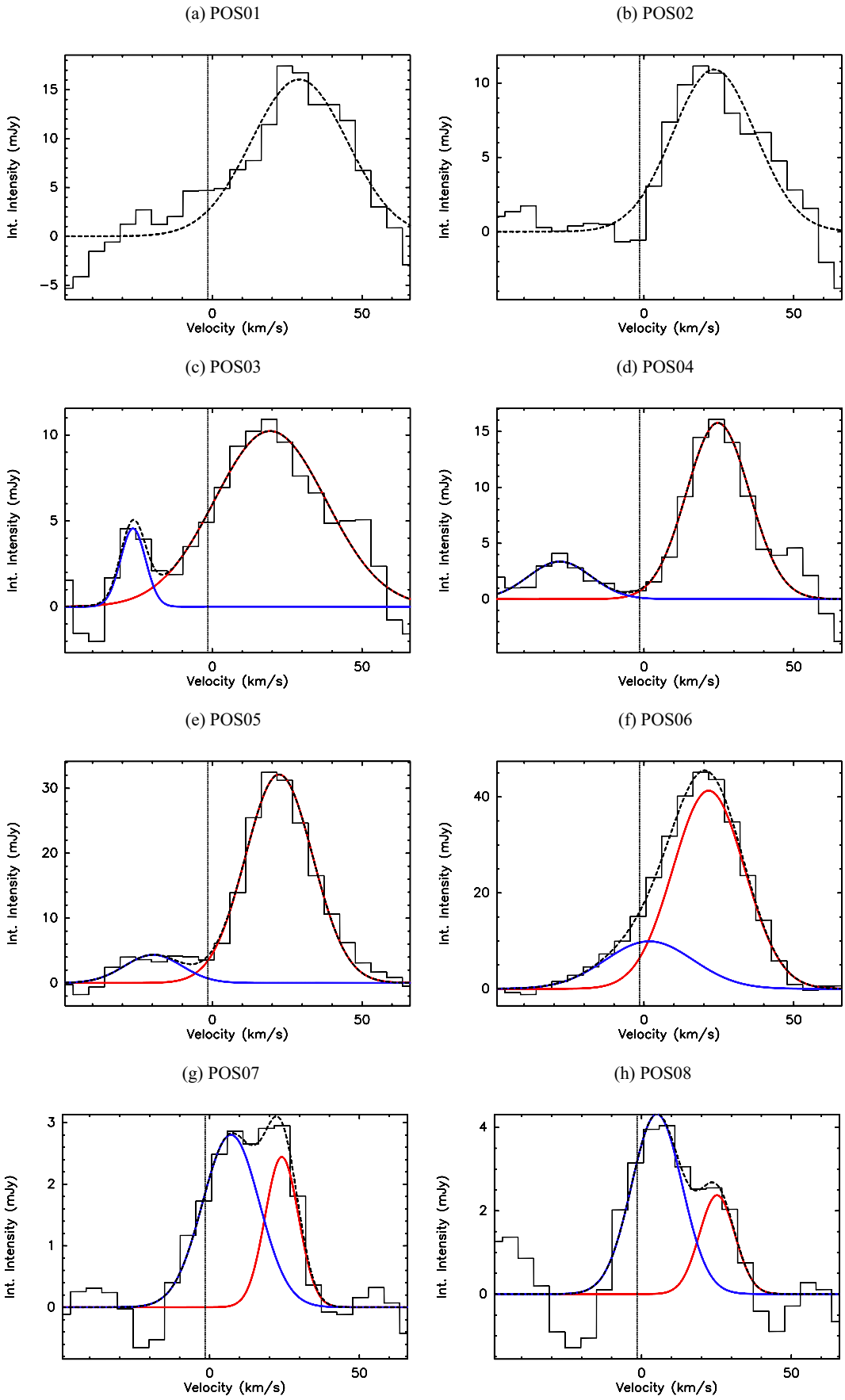

Fig. 4. H66α radio recombination line spectra. "Gaussian 1", the component with the higher velocity, is shown in red, and "Gaussian 2" in blue (Table 2). The dashed black line presents the sum of the two Gaussian fits. The vertical black line marks the systemic molecular gas velocity of -1.5 km s^{-1}.

(a) POS09

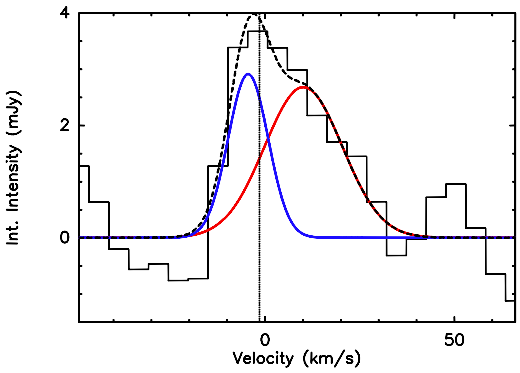

(b) POS10

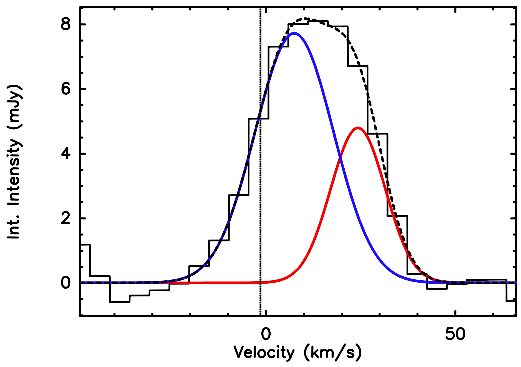

(c) POS11

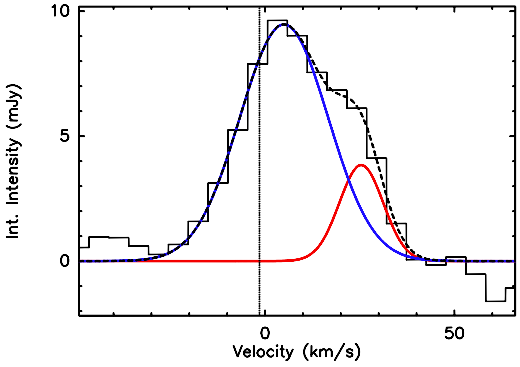

(d) POS12

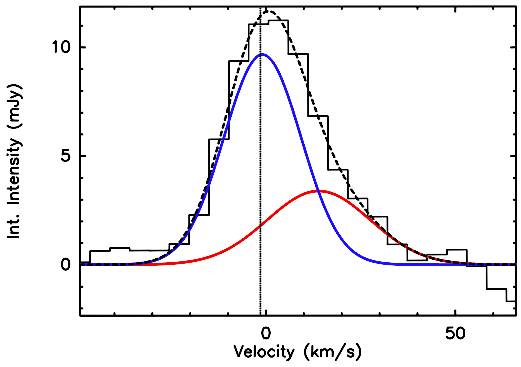

(e) POS13

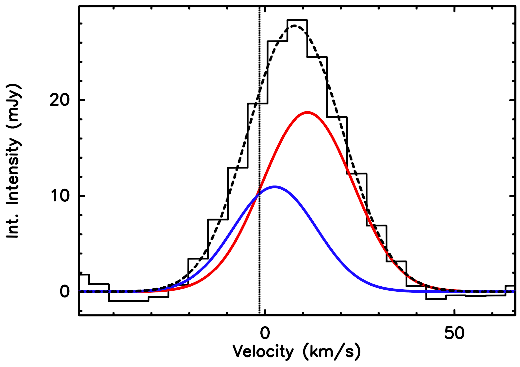

(f) POS14

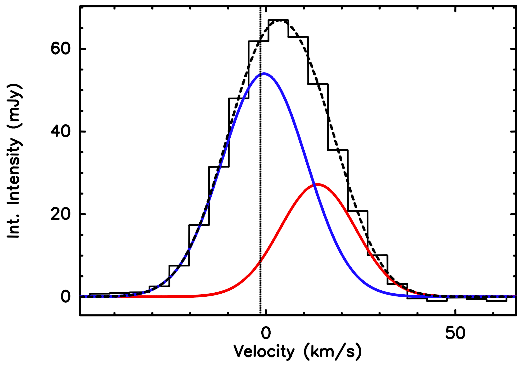

(g) POS15

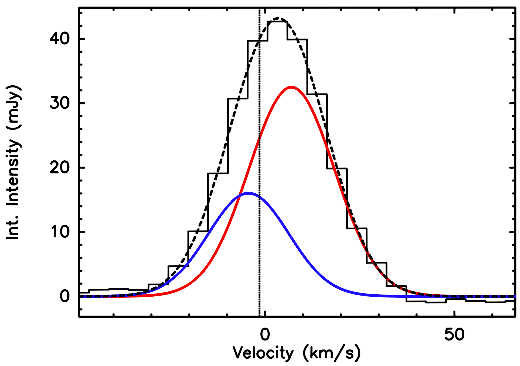

(h) POS16

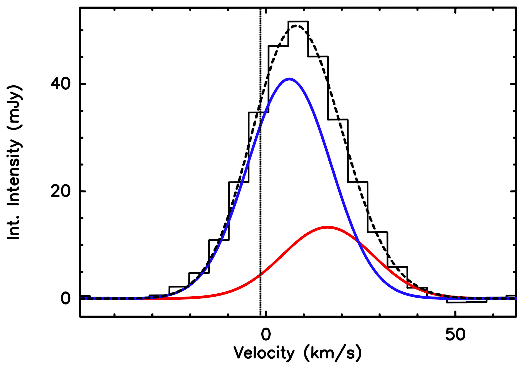

Fig. 4. continued.

(a) POS17

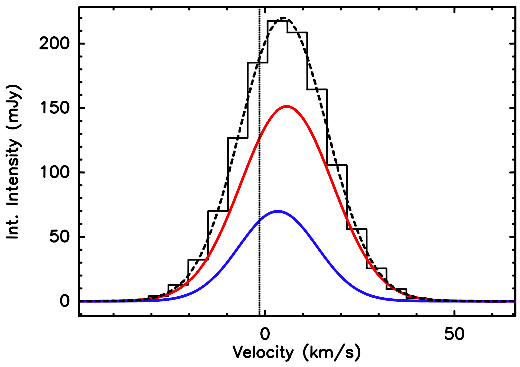

(b) POS18

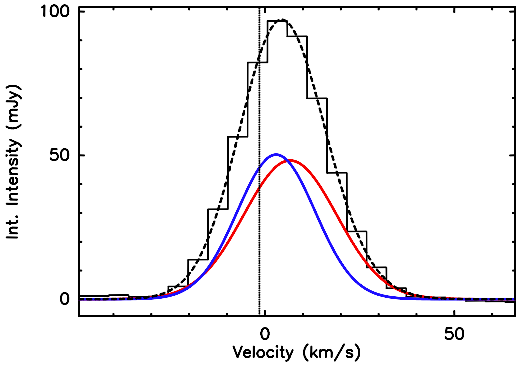

(c) POS19

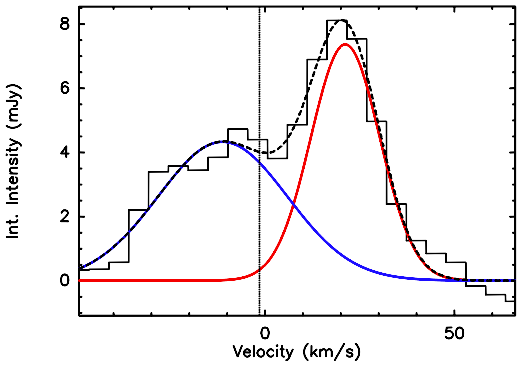

(d) POS20

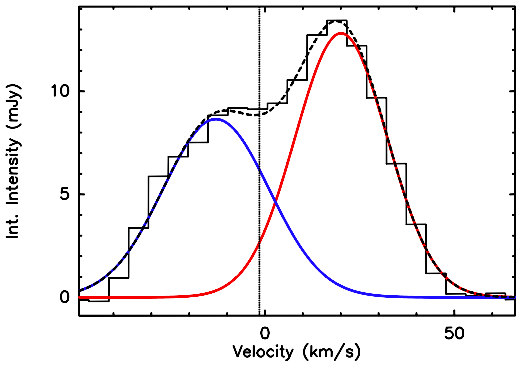

(e) POS21

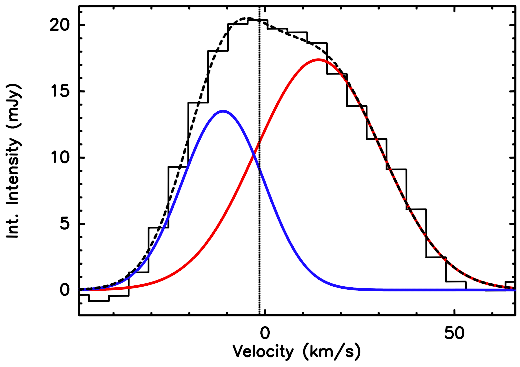

(f) POS22

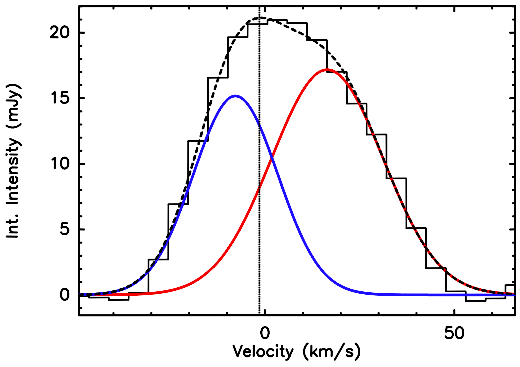

(g) POS23

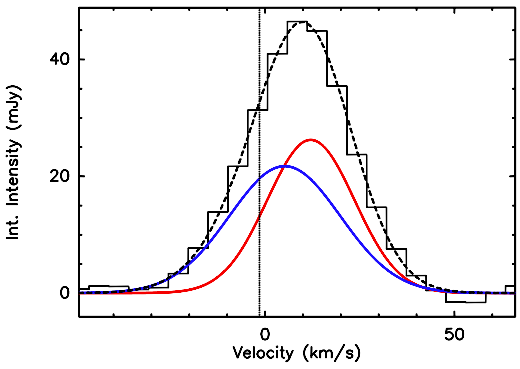

(h) POS24

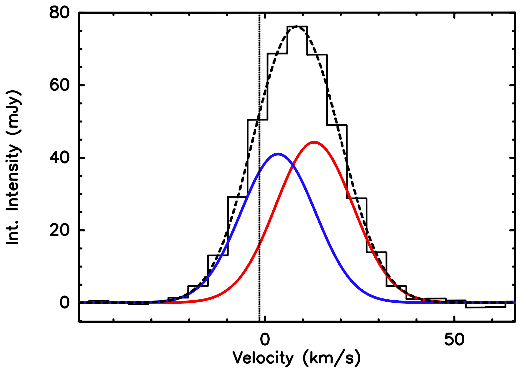

Fig. 4. continued.

(a) POS25

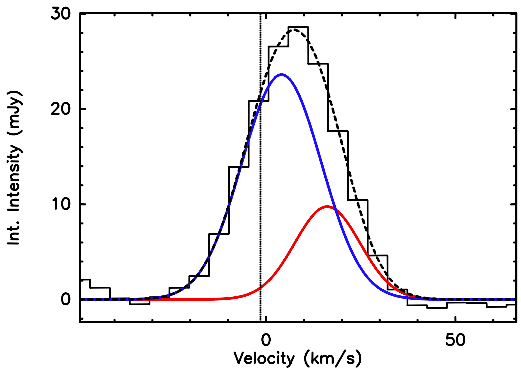

(b) POS26

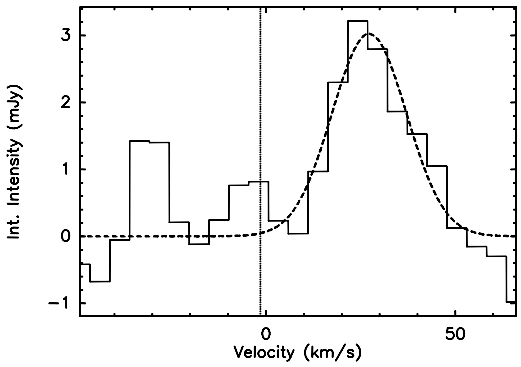

(c) POS27

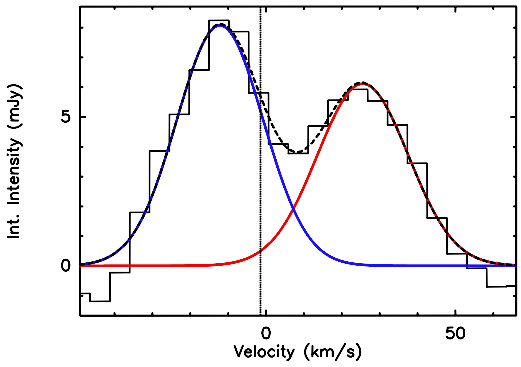

(d) POS28

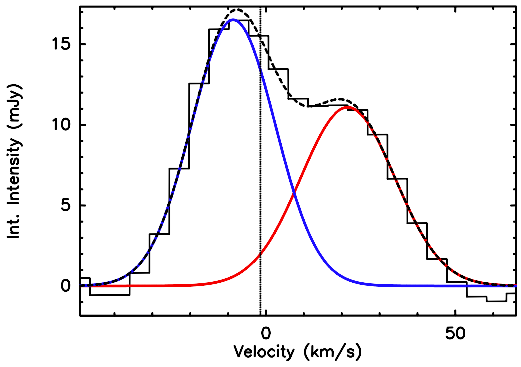

(e) POS29

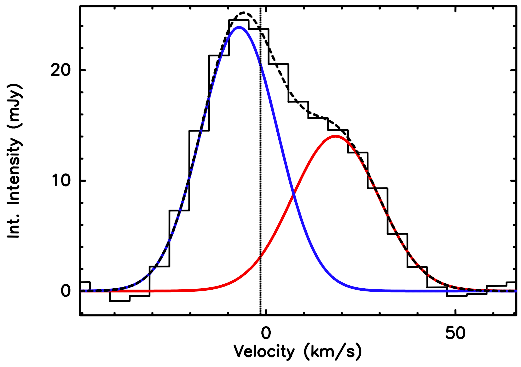

(f) POS30

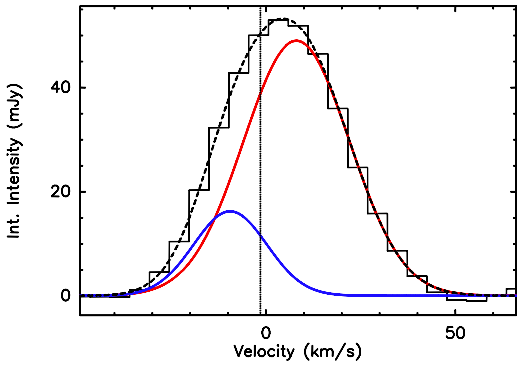

(g) POS31

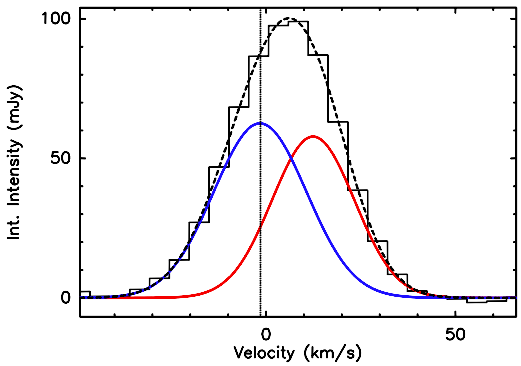

(h) POS32

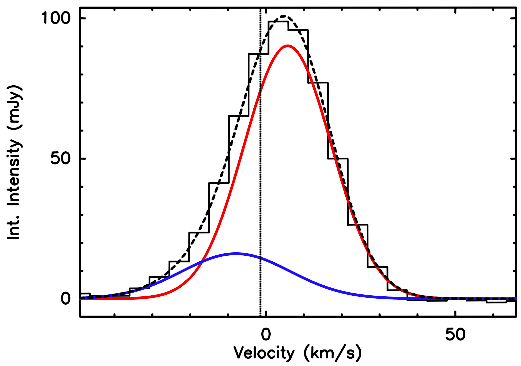

Fig. 4. continued.

(a) POS33

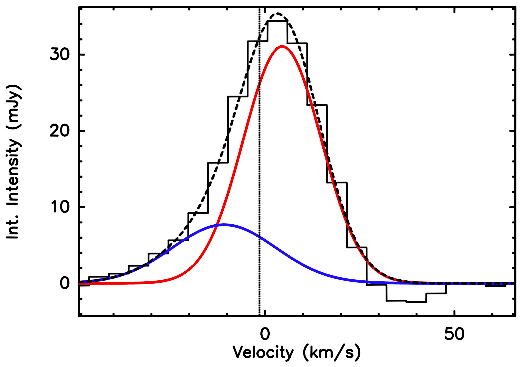

(b) POS34

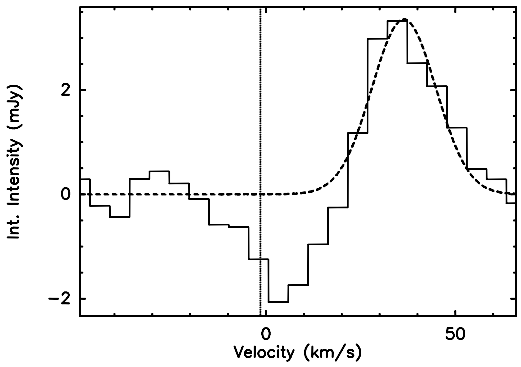

(c) POS35

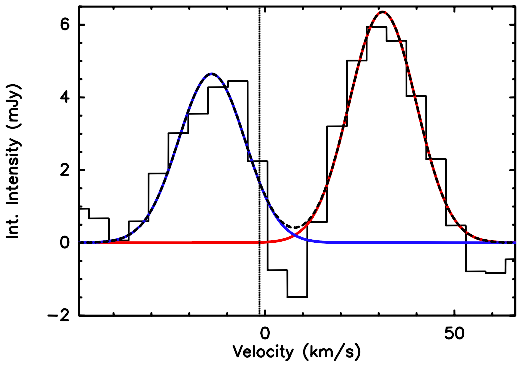

(d) POS36

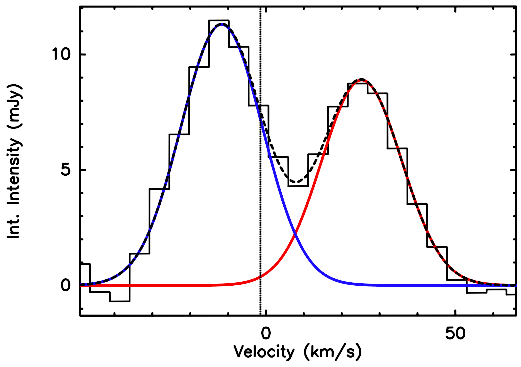

(e) POS37

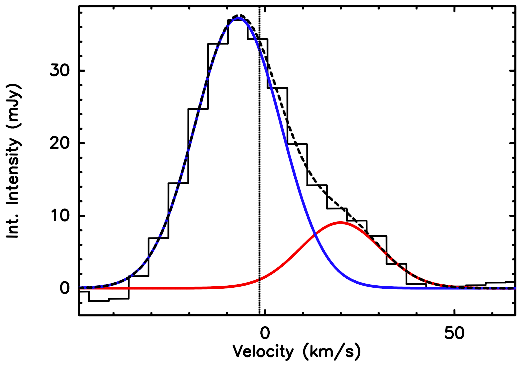

(f) POS38

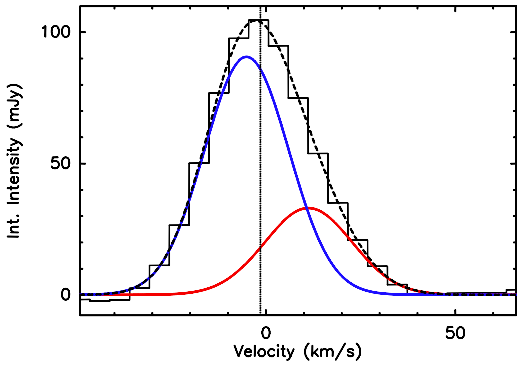

(g) POS39

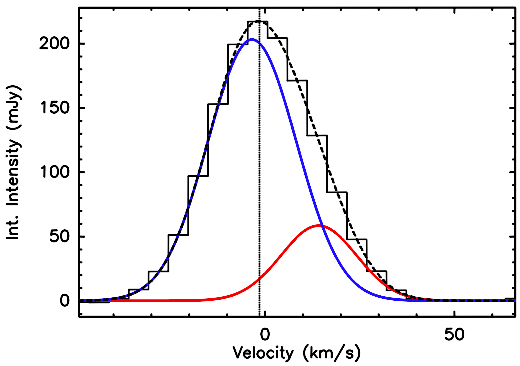

(h) POS40

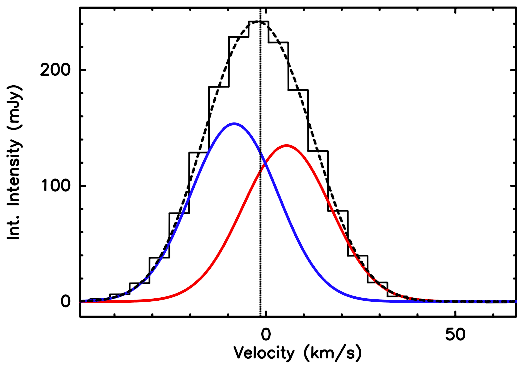

Fig. 4. continued.

(a) POS41

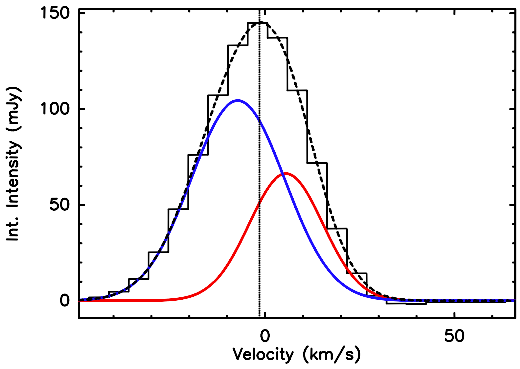

(b) POS42

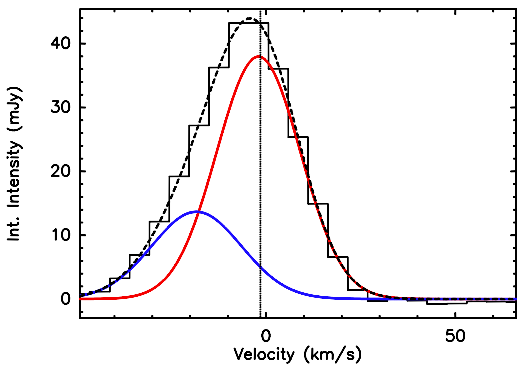

(c) POS43

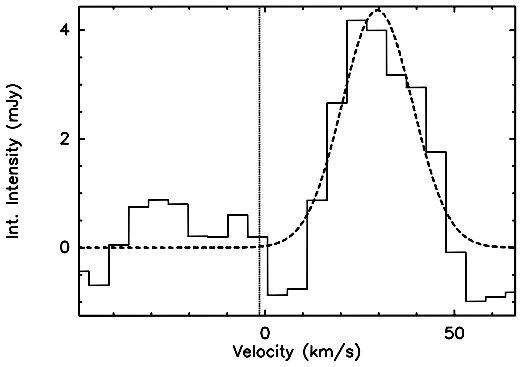

(d) POS44

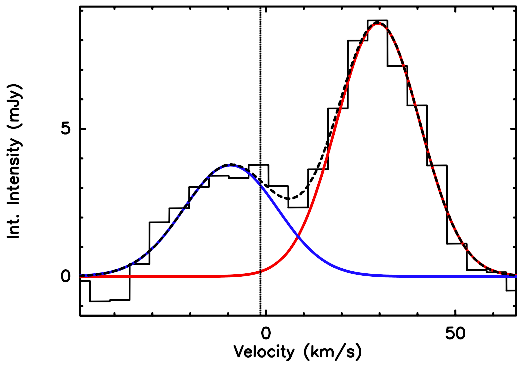

(e) POS45

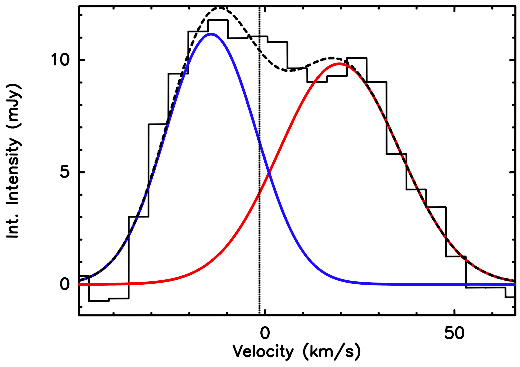

(f) POS46

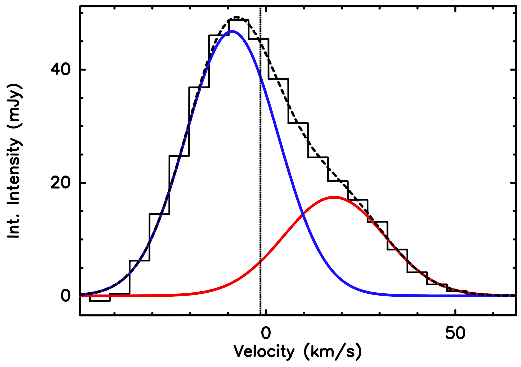

(g) POS47

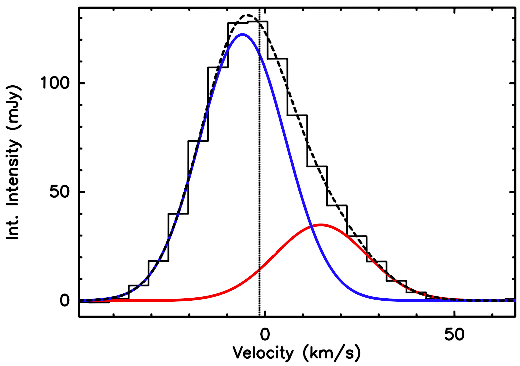

(h) POS48

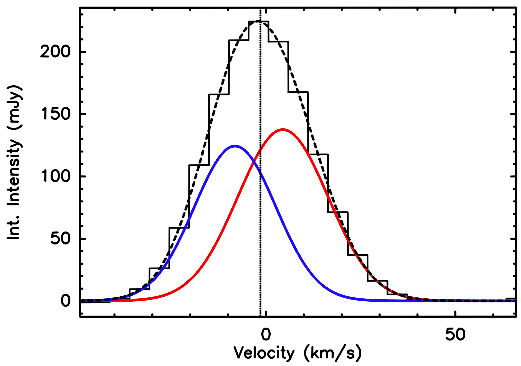

Fig. 4. continued.

(a) POS49

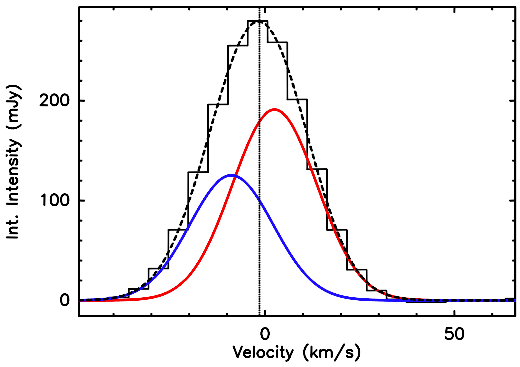

(b) POS50

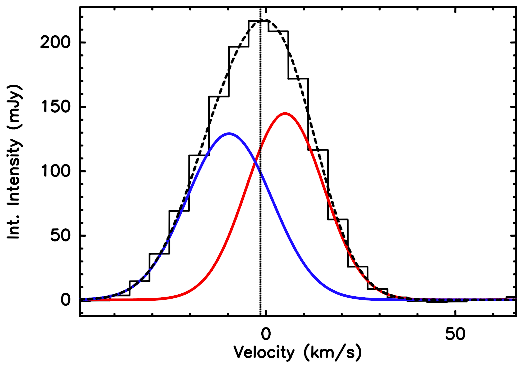

(c) POS51

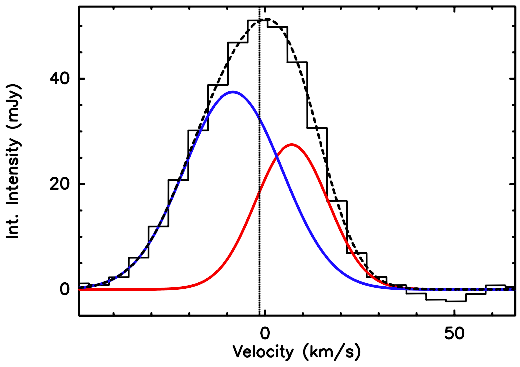

(d) POS52

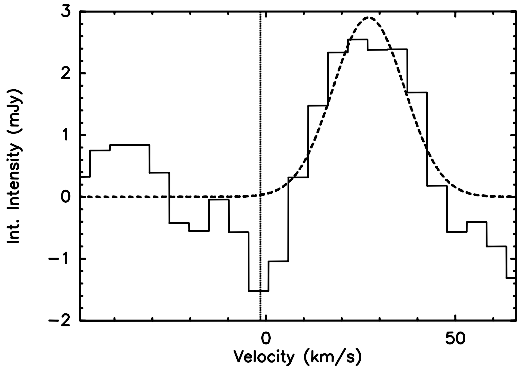

(e) POS53

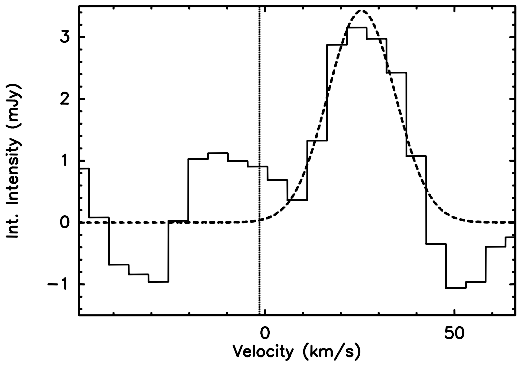

(f) POS54

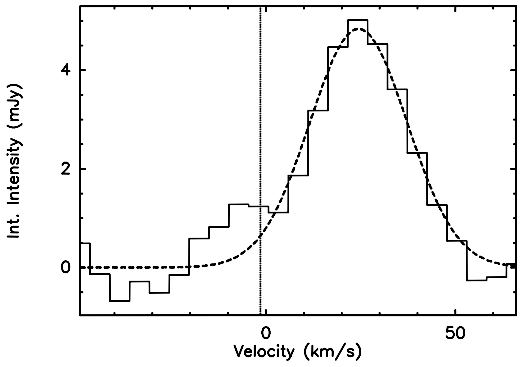

(g) POS55

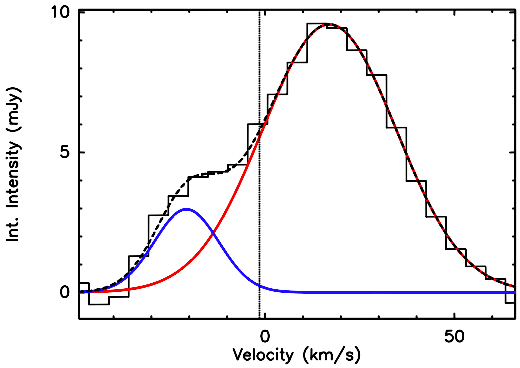

(h) POS56

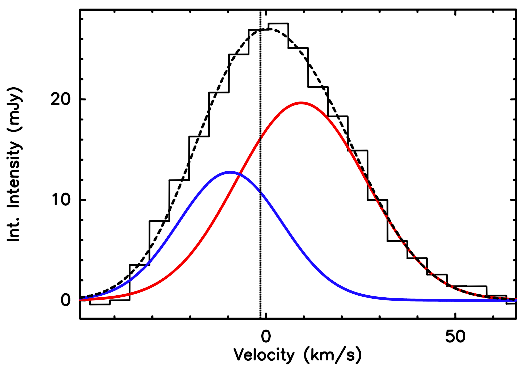

Fig. 4. continued.

(a) POS57

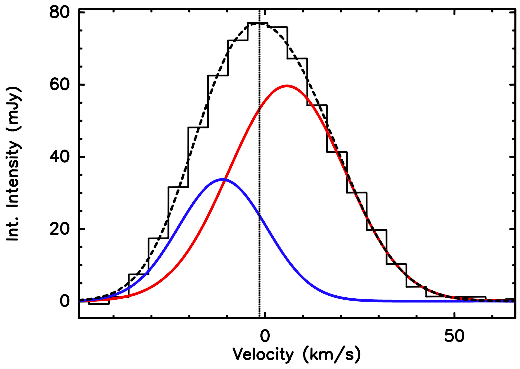

(b) POS58

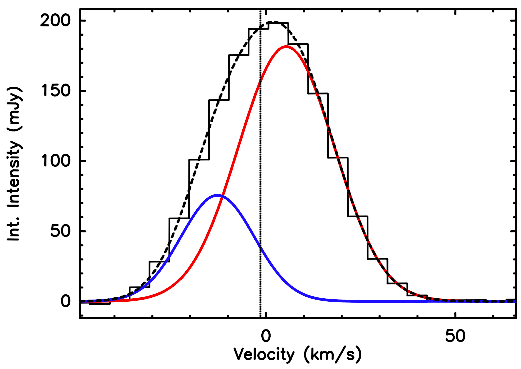

(c) POS59

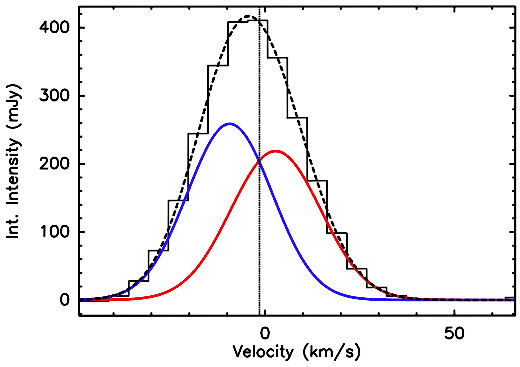

(d) POS60

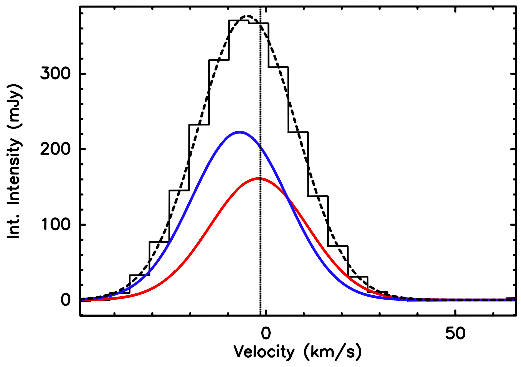

(e) POS61

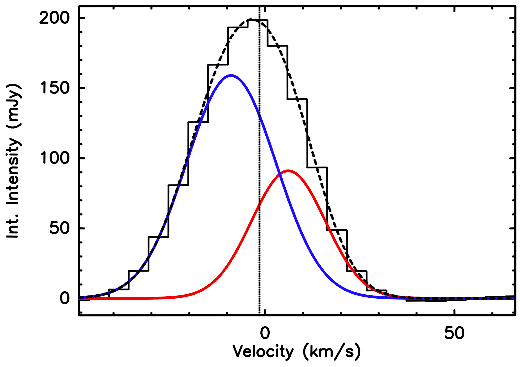

(f) POS62

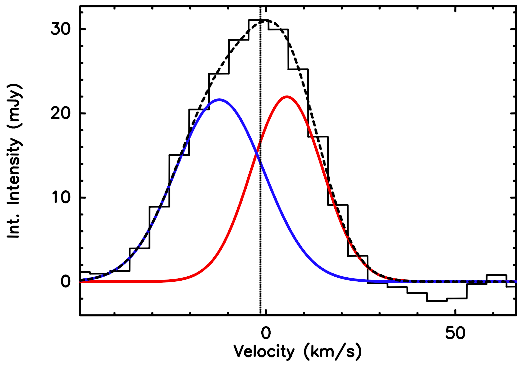

(g) POS63

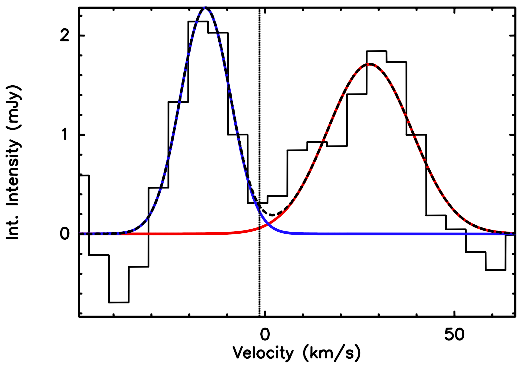

(h) POS64

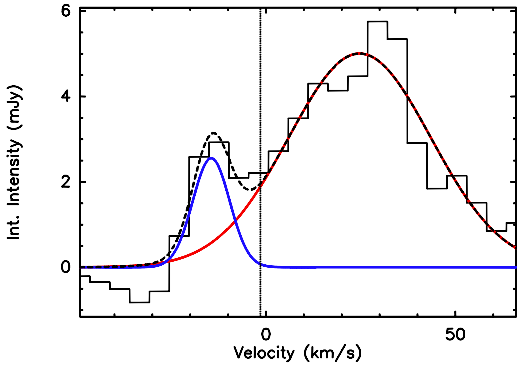

Fig. 4. continued.

(a) POS65

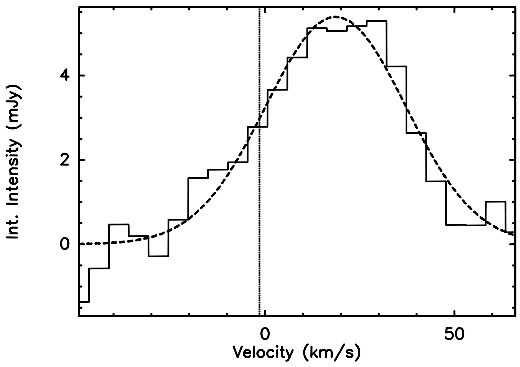

(b) POS66

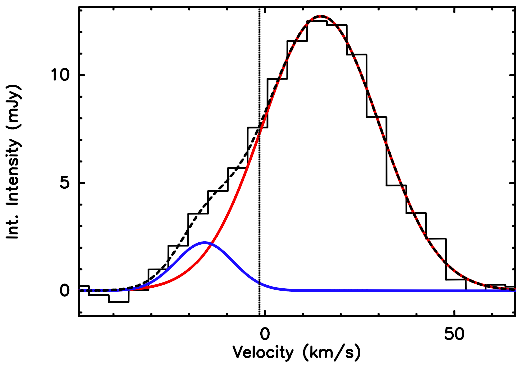

(c) POS67

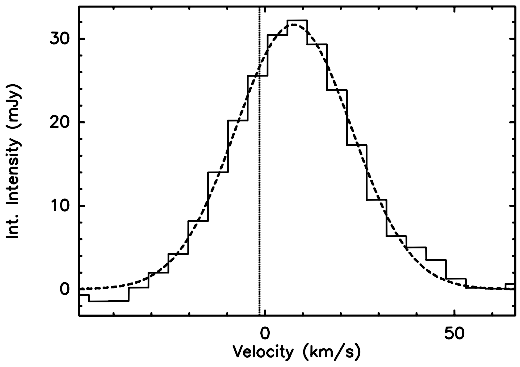

(d) POS68

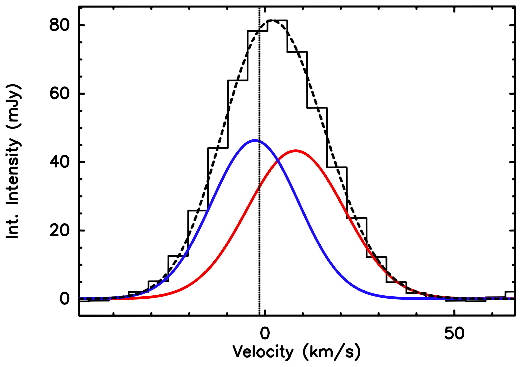

(e) POS69

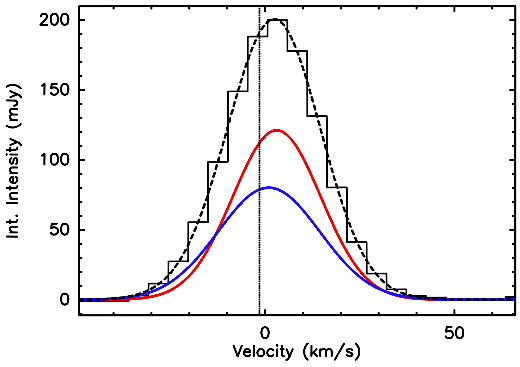

(f) POS70

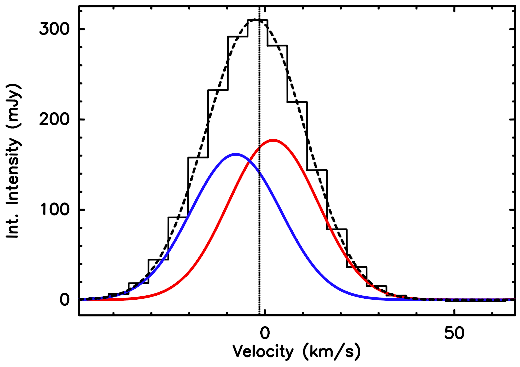

(g) POS71

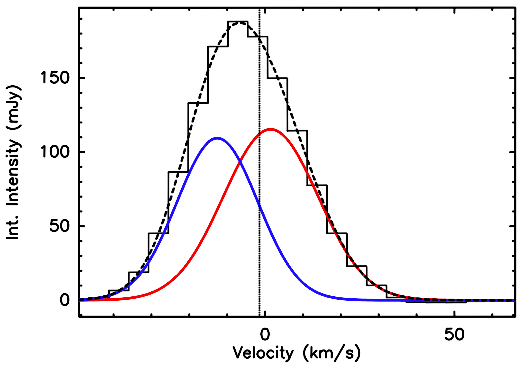

(h) POS72

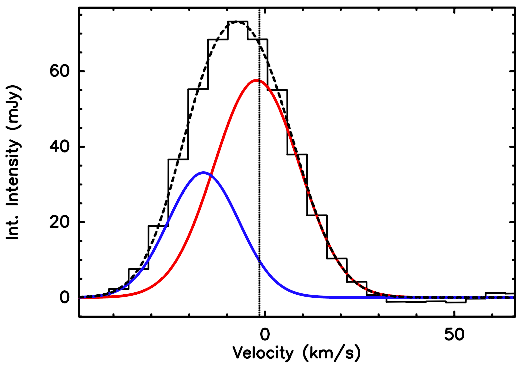

Fig. 4. continued.

Appendix A: Cometary H II region models

Since the publication of Paper I, the state of the art in compact H II region modeling has advanced considerably. Of particular relevance, Arthur & Hoare (2006) present four groups of radiation-hydrodynamic simulations of cometary H II regions:

i) Pure bow shock: stellar motion + stellar wind, no density gradient.
ii) Pure champagne flow: density gradient, no stellar wind, no stellar motion.
iii) Champagne flow + stellar wind: density gradient, stellar wind, no stellar motion.
iv) Champagne flow + stellar wind + stellar motion: density gradient, stellar wind, stellar motion.

We note that the schematic "hybrid" model proposed in Paper I (champagne flow and bow shock) is similar to (iv), but did not include a stellar wind.

For each of their models, Arthur & Hoare (2006) determine line intensity, mean velocity, and velocity dispersion at different positions in the H II region. For the bow shock model (model i), the velocities of the ionized gas at the head of the H II region are similar to the stellar velocity. Since the influence of the stellar motion on the gas is small in the tail, the velocities quickly converge to the systemic velocity of the surrounding material in this region. In the pure champagne flow model (model ii), the velocity of the ionized material at the position of the star is similar to the velocity of the ambient molecular material. Down the tail, the velocity of the ionized gas increases due to the drop in pressure. Including a stellar wind in the champagne flow model (model iii) causes the ionized gas to flow around the stellar wind bubble in a thin shell. The density gradient in the ambient material then leads to large accelerations at the sides of the flow. If additionally the star is moving up a density gradient (model iv), the direction of the flow between the ionization front and the stellar position changes (compared to the pure champagne flow model), being now in the direction of stellar motion (compare Figs. 3–5, and 12 of Arthur & Hoare 2006).

In all cases, the observed morphology and velocity structure will be affected by viewing angle. Zhu et al. (2008) consider viewing angle effects in some detail, in the context of [Ne II] 12.8 μm observations of a sample of compact and UC H II regions. In particular, for a cometary H II region viewed side-on (e.g., cometary axis in the plane of the sky), two velocity components are expected from a wind-confined ionized flow-one from the near and one from the far side of the paraboloidal shell (Figs. 46–47 of Zhu et al. 2008). At all positions, the two velocity components are symmetric about the velocity of the ambient gas. Notably, for this viewing angle it is not possible to distinguish between the bow-shock and pressure-driven stellar wind cases based on a position–velocity diagram. For intermediate viewing angles, two velocity components are expected near the head, while down the tail one velocity component (side of the shell) becomes dominant (Figs. 46, 47 of Zhu et al. 2008). The line-of-sight ionized gas velocities depend both on the precise viewing angle and on the model type. In contrast to the stellar-wind cases, in the wind-free champagne flow the ionized gas fills the "blister" cavity, limited by the ionization front. In this case, a single broad line is expected at all positions (Fig. 48 of Zhu et al. 2008).

Appendix B: General kinematics

To study the general kinematics of the DR 21 H II regions, we made individual channel maps of the continuum-free emission of the H66α line (Fig. B.1), showing emission between ±40 km s^{-1}. The RRL emission from the northern H II region generally covers a smaller velocity range than that from the southern H II region. Emission from the northern H II region peaks at ∼3 km s^{-1}, while the emission of the southern H II region peaks at ∼−7 km s^{-1}. At high positive velocities the north-east part of the southern H II region is more prominent whereas its south-west part is more prominent at high negative velocities.

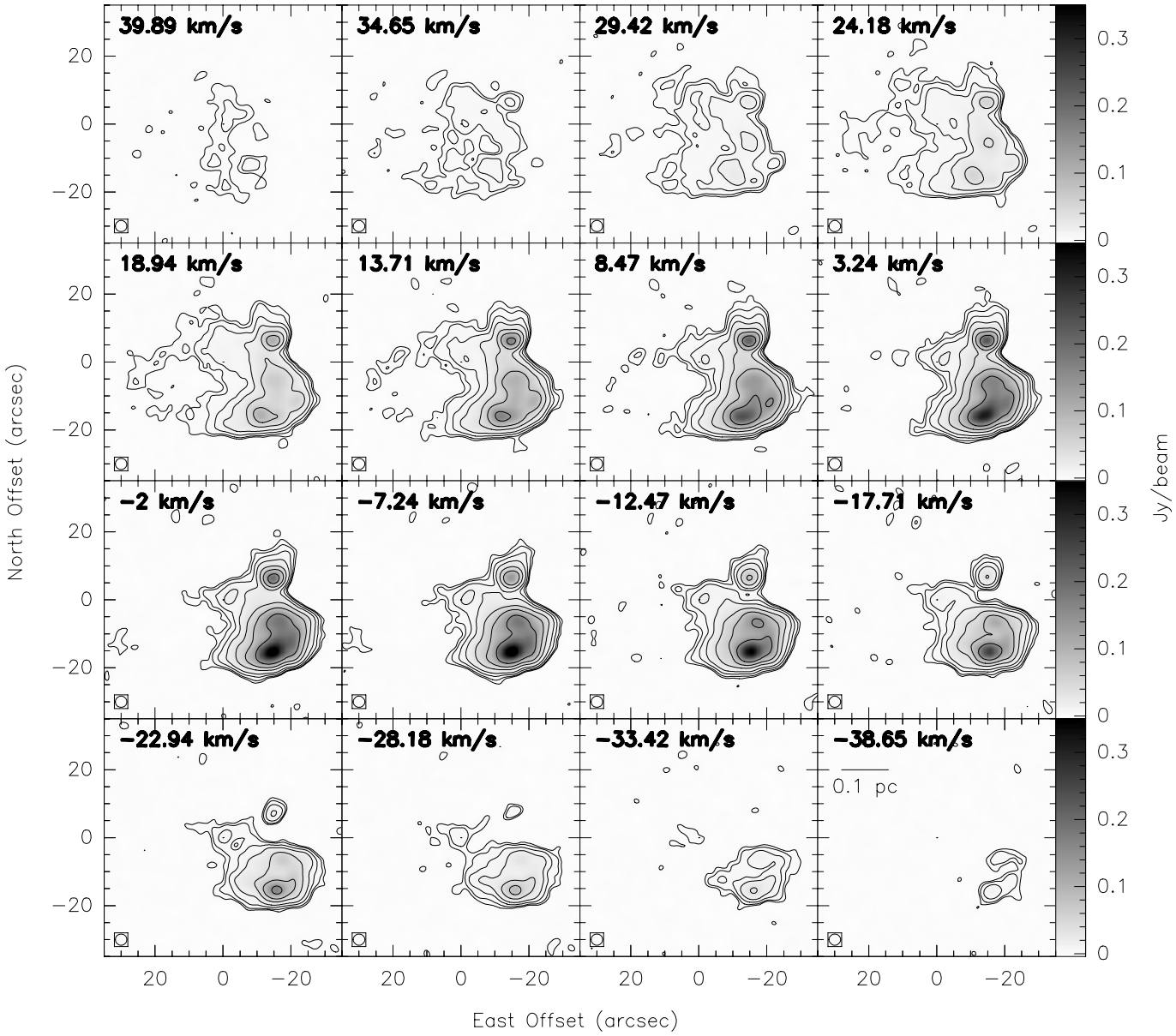

Fig. B.1. Individual channel maps of the H66α line emission, showing every channel between 40 and −39 km s^{-1}. The velocity of each channel is given in the upper left corner of each plot. The contour levels are at 3σ, 5σ, 10σ, 20σ, 50σ, 100σ, 200σ, and 500σ (1σ = 0.7 mJy beam^{-1}). The image shows the inner $(1')^2$ of the primary beam. The 3.4″ synthesized beam is shown in the lower left corner of each channel map. A scale of 0.1 pc is shown in the lower right channel map. The (0, 0) position is at RA(J2000) = 20h 39m 02.557s and Dec(J2000) = 42d 19′ 47.2″.